Detection of near-wall vortices and their manipulation by use of dielectric barrier discharge plasma actuators

Ryan Connelly

A thesis submitted in partial fulfillment

of the requirements for the degree of

Master of Science in Aeronautics & Astronautics

University of Washington

2017

Committee:

Robert Breidenthal

Carl Knowlen

Program Authorized to Offer Degree:

Aeronautics & Astronautics

University of Washington

Abstract

Detection of near-wall vortices and their manipulation by use of dielectric barrier discharge plasma actuators

Ryan Connelly

Chair of the Supervisory Committee:
Professor Robert Breidenthal
Aeronautics & Astronautics

A sizable amount of the drag on a typical jet airplane is due to skin friction. Decreasing this skin friction drag by even just a small percentage could significantly increase the efficiency of the plane. The idea of stationary vortices has previously been proposed as a method of skin friction reduction. Vortices could potentially be held stationary by flow control devices such as plasma actuators. This thesis lays the groundwork of a study to determine the feasibility of this idea in two ways. First, the effects of plasma actuators on vortices are studied. Second, wind tunnel tests were performed to develop a method of locating the center of vortices downstream of vortex generators. An accurate method of vortex detection will be vital in further experimental studies of plasma actuator effects.

TABLE OF CONTENTS

Page

LIST OF FIGURES

LIST OF TABLES

ACKNOWLEDGMENTS

I would first like to thank my advisor, Dr. Robert Breidenthal, for sharing his expertise on the subject and his guidance over the past year and a half. His time and patience were invaluable in helping me to understand the subject matter. I would also like to thank Dr. Giovanni Nino for the countless commutes across the city to meet and discuss the project. I am grateful to them both for providing the opportunity to work on this project.

I would also like to express my gratitude to Dr. Carl Knowlen for taking the time to review my thesis and provide valuable input.

The wind tunnel tests would not have been possible without the help of many individuals. Jack Ross and the rest of the Kirsten Wind Tunnel crew were very accommodating and provided crucial assistance throughout the setup and testing. Tim Sundine put in numerous hours as an undergraduate volunteer to help prepare the model. Eagle Harbor Technologies was extremely generous in providing equipment necessary to operate the plasma actuators.

Most importantly, I would like to thank my family for their support. I would not have made it this far without everything you have done.

Chapter 1

INTRODUCTION

1.1 Flow Separation

Flow separation in a laminar boundary layer occurs due to a positive pressure gradient in the, $\frac{dp}{dx} > 0$. The streamlines in a boundary layer are parallel to the wall and straight. Therefore in the case of a flat wall, no y-components are considered and $\frac{dp}{dy} \cong 0$. Ignoring friction, the Euler equation is

$$dp = -\rho u du. \tag{1.1}$$

For any two locations in x, fluid near the top of a boundary layer will have a relatively large u compared to fluid near the wall. For equation 1.1 to be valid, du will remain small. Conversely, the fluid near the wall has a very small u, requiring a large du to account for the pressure gradient, dp. The non-linearity of the Euler equation leads to a very quick loss of momentum near the surface, eventually leading to separation.

Vortex generators are commonly used as a passive way to delay this separation. Vortex generators come in a large variety of geometries, but they all achieve results by the same mechanism. Each generator creates a vortex in the boundary layer, just above the surface. The rotation of the fluid in the vortex replaces low-momentum fluid near the wall with high-momentum fluid from near the edge of the boundary layer. This momentum transfer decreases the velocity gradient in y and delays separation.

Delaying separation has obvious advantages, such as increasing stall angle of attack. But another, potentially more advantageous effect of vortex generators is that they can delay the laminar to turbulent transition, leading to decreased skin friction drag [1] For a typical jet airplane, a large amount of the drag is due to skin friction. Reducing this skin friction by a small percentage could lead to a very significant increase in efficiency.

1.2 Stationary Vortices

Vortices near a surface are unstable due to long-wave Crow instabilities and short-wave Widnall instabilities. They also have a tendency to drift along a surface due to an image vortex inducing a velocity at the real vortex. For the case of a single vortex above a flat surface, this velocity is

$$v_{drift} = \frac{\Gamma}{4\pi h}. \tag{1.2}$$

The derivation of this equation is described in Chapter 3. Cotel [3, 4] has shown that stationary or stable vortices behave differently than in the typical, nonstationary case. The stationary vortices could significantly reduce the entrainment rate and surface fluxes [5] while decreasing skin friction drag [6].

The effects of stationary vortices have been tested by using a wavy wall. In potential flow, any streamline could be replaced with a surface. So a stationary vortex configuration, such as Kelvin cat's eye flow, could be recreated along a surface by using a wavy wall to approximately simulate the lower separatrix, as shown in Figure 1.1. Theoretically, vortices placed in the troughs of the wall should remain stationary. Experimental observations have proven this vortex persistence as well as the reduced surface fluxes. Further, Ranjan and Breidenthal [6] created an airfoil with a wavy surface to test for delayed boundary layer separation and reduced skin friction drag. Experimental results have all so far been in accord with the theory.

In practical applications, the drawbacks of this wavy surface airfoil would probably outweigh the benefits. The size and geometry of the ridges were designed for very specific operating conditions. With any slight change in yaw angle, the vortices may no longer be in the center of the valleys as they were designed. One potential solution is to utilize plasma actuators in a similar way that could replace the wavy wall.

Plasma actuators are attractive for flow control because they can be used to induce momentum in the boundary layer nearly parallel to the surface while minimally interfering with the flow due to their small thickness. They have successfully proven effective in delaying separation when directly adding momentum to the primary flow, as seen in Figure 1.2. Plasma actuators could potentially be used as a method to add momentum to the secondary

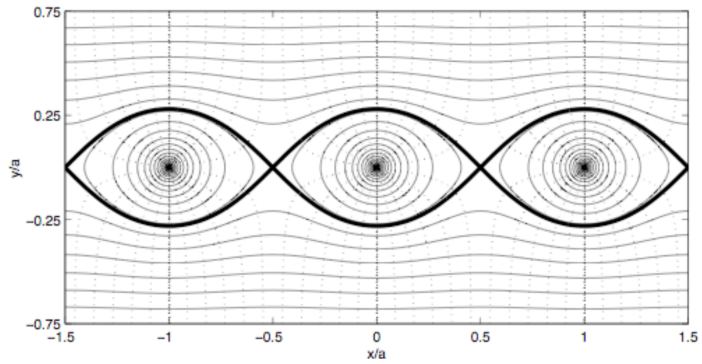

Figure 1.1: Example of streamlines of a Kelvin cat's eye flow. This stationary vortex configuration could be produced above a surface by approximately recreating the lower half of the separatix with a wavy wall. [7]

flow of a vortex to simulate the effects the wavy wall without the drawbacks. Furthermore, Bauer [8] has shown that the wavy wall only relaminarizes the flow over one half of the wavy wall wavelength, where the flow is accelerated. The half where deceleration occurs remains turbulent. Plasma actuators may be able to improve on this by accelerating the fluid over the entire surface, thereby creating a laminar boundary layer over the entire surface.

The following chapters discuss two requirements of a system to control the flow in vortices: the actuators themselves and a method to detect the location of the vortices. Previous research and literature on plasma actuators was studied to determine the best type of actuator for such a system and the parameters that could be tuned to generate the ideal flow. In addition, an experimental study was performed to determine minimum pressure sensor requirements to accurately locate the center of a vortex downstream of a vortex generator.

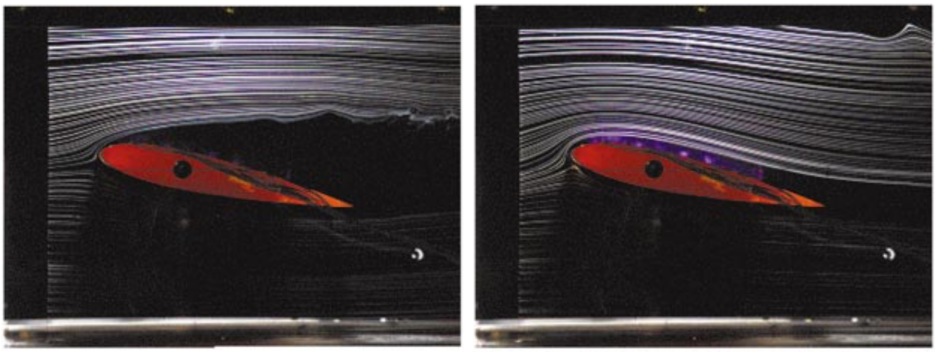

(a) Plasma off. (b) Plasma on.

Figure 1.2: Example of flow separation control possible by use of plasma actuators. [2]

Chapter 2

PLASMA ACTUATORS

2.1 Background

Two common types of plasma actuators are corona discharge actuators and dielectric barrier discharge (DBD) actuators. Corona discharge actuators consist of an anode and cathode separated by a small air gap. There is no specific geometry for corona discharge actuators. Various sizes and numbers of electrodes could be used depending on the application. If an anode and cathode are separated in space, the actuator is referred to as a volume corona. Surface coronas, on the other hand, consist of the electrodes fixed to a surface. Regardless of the configuration, the mechanism works the same way. High voltage positive direct current is applied to the anode, while the cathode is grounded. A plasma is formed between the two electrodes. The high velocity movement of the ions in this plasma is transferred to the fluid through collisions, creating a so-called 'ionic wind' and adding momentum to the flow. The maximum velocity measured with a corona discharge actuator has been $5m/s$ [9].

The geometry of DBD plasma actuators is similar to that of surface coronas, but they include a thin dielectric layer between the two electrodes, as shown in Figure 2.1. Rather than direct current, a high voltage alternating current is applied. Generally DBD actuators use a sinusoidal AC input, but many other waveforms, such as sawtooth and square waves, have been used to improve on specific characteristics [10]. It may seem that in the case of a pure sinusoidal input, there would be no net induced flow in the fluid. But, due to the asymmetric geometry of the actuator, there is a clear net flow. In the negative-going half-cycle, electrons originate from the exposed electrode and move towards the dielectric. This is a virtually infinite source of electrons and readily gives them up. Conversely, in the positive-going half-cycle, the electrons originate from surface of the dielectric. The dielectric only contains the electrons that moved there during the previous half-cycle. Due to the limited number, these electrons do not come off as readily. Once a certain voltage

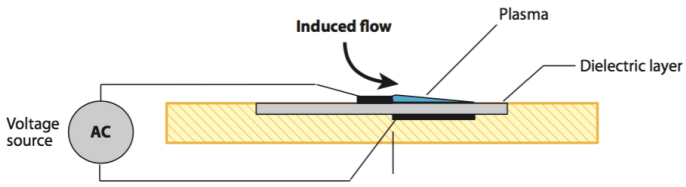

Figure 2.1: Diagram showing the geometry of a DBD plasma actuator. [12]

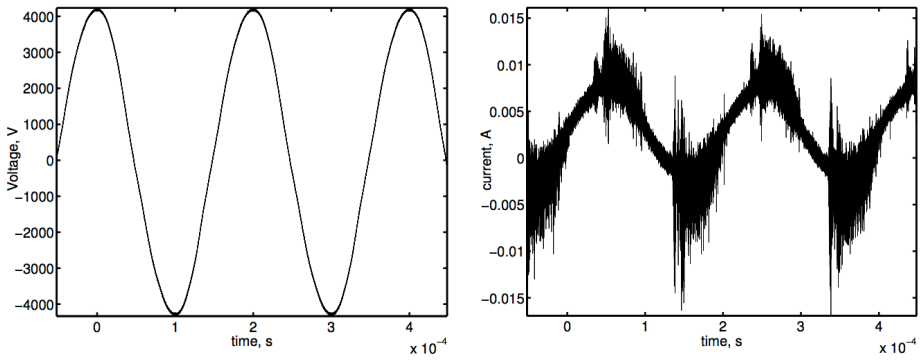

Figure 2.2: Comparison of voltage and current measurements during operation of an ac-DBD plasma actuator. [13]

threshold is reached, plasma is formed between the two electrodes, typically in the form of quick microdischarges. Figure 2.2 compares the input voltage with the measured current. The discussed microdischarges and asymmetry can be clearly observed in this figure. The microdischarges only occur over part of the period and are significantly larger in the negative-going half-cycle. This is backed up further in Figure 2.3, which shows the voltage signal and the photo-multiplier tube (PMT) output. The PMT output is proportional to light intensity, which corresponds to the amount of plasma present at a given time. [11]

DBD actuators generally show more promise for flow control applications because the induced velocity is greater than that of corona discharge actuators for the same power and is in a direction parallel to and very near the surface where the actuator is applied. The velocity induced by a corona discharge actuator acts farther from the wall and includes components away from the wall, which is not preferable for most flow control applications.

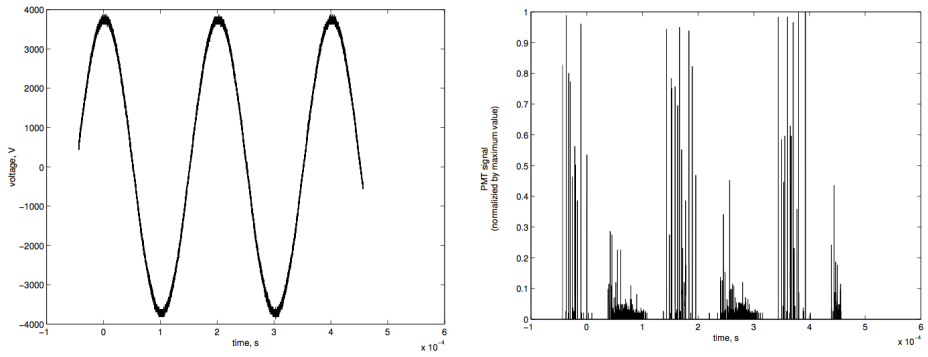

Figure 2.3: Plot of the input voltage and the light intensity measured by a photo-multiplier tube. The light intensity corresponds with the plasma intensity. [11]

Figure 2.4 compares the velocity profiles of a corona discharge and DBD actuator. [9]

The geometric configuration of an ac-DBD plasma actuator plays a significant role in the performance of the actuator. The maximum induced velocity near the surface, v_{max} is arguably the most important property of the output. This velocity increases asymptotically with the width of the covered electrode when the voltage is held constant, as shown in Figure 2.5a. Interestingly, the geometry of the exposed electrode has a nearly negligible effect on the properties. [10] For a fixed voltage, U_{max} is related to the gap between the electrodes, d, by a parabolic-like curve with a optimum spacing to provide the maximum velocity, as shown in Figure 2.5b. Increasing the gap accelerates the electrons over a longer distance, but at a certain point, the decreased electric field due to the larger dielectric between the two electrodes causes the velocity to drop. Increasing the dielectric thickness, or similarly decreasing the permittivity, results in a decrease in U_{max} but increases the stability of the actuator. [15]

Besides the geometric configuration, the other factor to significantly affect the actuator's performance is the input waveform. While the general shape of the wave could be altered to tailor the output, most research focuses on a sinusoidal. For a sine wave, the maximum velocity is proportional to $V^{\frac{7}{2}}$ [12] and directly proportional to the frequency. [16] Measurements showing the velocity increase throughout the boundary layer with voltage are shown

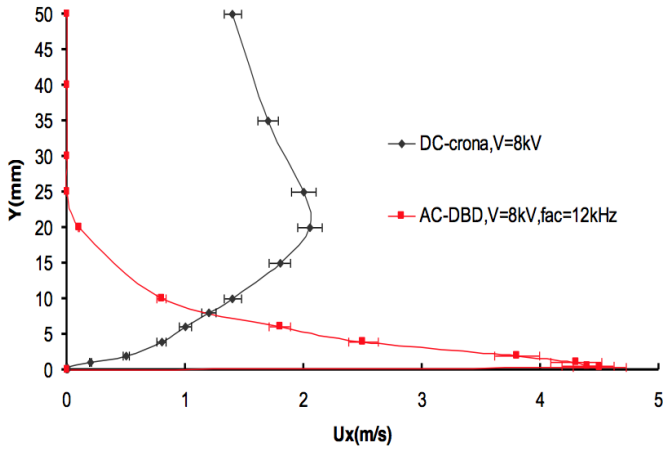

Figure 2.4: Comparison of the x-velocity profiles induced above a surface by a corona discharge actuator and a DBD actuator with similar properties. [14]

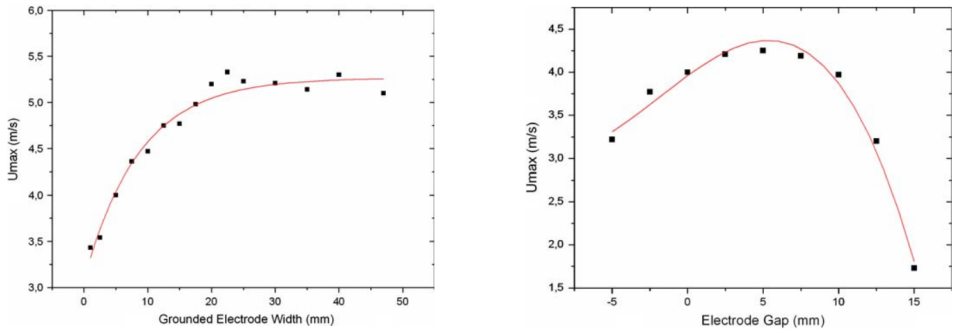

(a) (b)

Figure 2.5: Plots of the maximum induced velocity, U_{max}, as a function of (a) grounded electrode with and (b) electrode gap. [15].

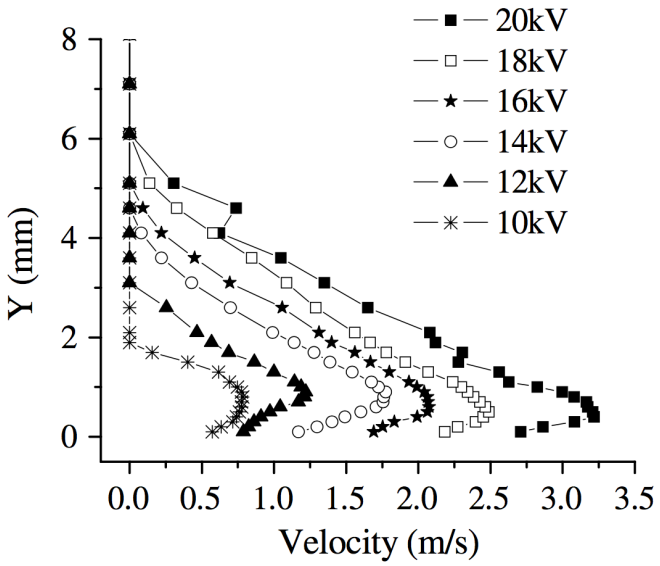

Figure 2.6: Velocity profiles over the surface of a wall for an ac-DBD plasma actuator at various peak input voltages. [9]

in Figure 2.6.

While most research on DBD plasma actuators has utilized AC current (ac-DBD), recent research has begun to focus on DBD plasma actuators which are powered by nanosecond-pulsed current, or ns-DBD plasma actuators. The geometry of ns-DBD actuators is identical to that of ac-DBD actuators and the influence on the fluid is very similar. But, the physics behind their operation is different. The input for ns-DBD plasma actuators consists of very quick pulses of high voltage current. The resulting strong electric field dissociates the particles, exciting the translational degree of freedom and increasing the temperature locally. This happens quickly enough that the air does not have adequate time to expand. Therefore, the pressure rises, followed by an adiabatic expansion driving a shockwave [17]. This expansion is responsible for the the induced flow, rather than an ionic wind as with most other types of plasma actuators. Experiments have proven ns-DBD plasma actuators to be highly efficient compared to ac-DBD plasma actuators [18].

2.2 Modeling

A numeric DBD plasma actuator model that can accurately model the ionic wind induced in the flow and can be parametrically altered would be an invaluable tool in future plasma actuator studies. One such model was developed by Suzen *et al.* [19]. This Suzen model involves a relatively simple formulation and provides sufficiently accurate results for many cases. The model computes both the electric potential due to an AC input voltage and the charge density representing the ion motion across the domain. The results of these two solutions are used to calculate body forces that can then be applied to a flow solver.

The Suzen model attempts to determine the electrohydrodynamic (EHD) force enacted on the fluid by the plasma. Ignoring any magnetic effects, this force can be represented by

$$\vec{f}_B = \rho_c \vec{E}, \tag{2.1}$$

where ρ_c and $\vec{E}$ are the charge density and electric field, respectively. The electric field is the negative gradient of the potential, or

$$\vec{E} = -\nabla\Phi. \tag{2.2}$$

Using this definition of $\vec{E}$, Gauss's Law can be rewritten

$$\nabla \cdot (\varepsilon \nabla\Phi) = -\rho_c, \tag{2.3}$$

where ε, the permittivity, is the product of the permittivity of free space, ε_o, and the relative permittivity of the medium, ε_r:

$$\varepsilon = \varepsilon_o \varepsilon_r. \tag{2.4}$$

In the plasma created by a plasma actuator, there is only weak ionization of the gas particles. The Suzen model takes advantage of this to decouple the electric potential into two parts: the potential due to the electric field, ϕ, and the potential due to the charge density in the plasma, φ:

$$\Phi = \phi + \varphi. \tag{2.5}$$

These two potentials could now be solved for independently of the other. From equation 2.3, the two equations used to solve the two potentials become

$$\nabla \cdot (\varepsilon_r \nabla\phi) = 0 \tag{2.6}$$

and

$$\nabla \cdot (\varepsilon_r \nabla \varphi) = -\frac{\rho_c}{\varepsilon_o}. \tag{2.7}$$

Potential is related to charge density by

$$\varphi = -\frac{\rho_c \lambda_d^2}{\varepsilon_0}, \tag{2.8}$$

where λ_d is the Debye length, which describes a radius of a sphere in a plasma where an ion is not electrically screened by ions of opposite sign. Equation 2.7 can then be rewritten

$$\nabla \cdot \left[\varepsilon_r \nabla \left(-\frac{\rho_c \lambda_d^2}{\varepsilon_o} \right) \right] = -\frac{\rho_c}{\varepsilon_o}. \tag{2.9}$$

Because the charge only builds up in the air region, the relative permittivity is constant. ε_o and λ_d can be removed from the gradient, leaving the charge density equation in the form of a Poisson equation:

$$\nabla^2 \rho_c = \frac{1}{\varepsilon_r \lambda_d^2} \rho_c. \tag{2.10}$$

Far from the actuator, the charge density goes to 0, so the boundary condition $\rho_c = 0$ is applied to the far-field bounds. At the surfaces of the dielectric and the exposed electrode, the Neumann boundary condition $\frac{\partial \rho_c}{\partial n} = 0$ is applied. On the dielectric surface directly above the covered electrode, the charge density boundary condition is set as a function of x and t,

$$\rho_{c,w}(x,t) = \rho_c^{max} G(x) f(t), \tag{2.11}$$

where ρ_c^{max} is the maximum charge density, $f(t)$ is the wave function of the AC input, and $G(x)$ is a Gaussian function that approximates the spatial distribution of the charge across the surface as

$$G(x) = \exp\left[-\frac{(x-\mu)^2}{2\sigma^2} \right]. \tag{2.12}$$

x is the distance from the edge of electrode closest to the exposed electrode, for $x \geq 0$, μ is set to zero to position the peak of the Gaussian at the $x = 0$, and σ is a constant that controls the spatial decay rate. In operation, most of the charge collects above the covered electrode, near the exposed electrode with a decay as the distance from the exposed electrode increases. These boundary conditions are summarized in Figure 2.7.

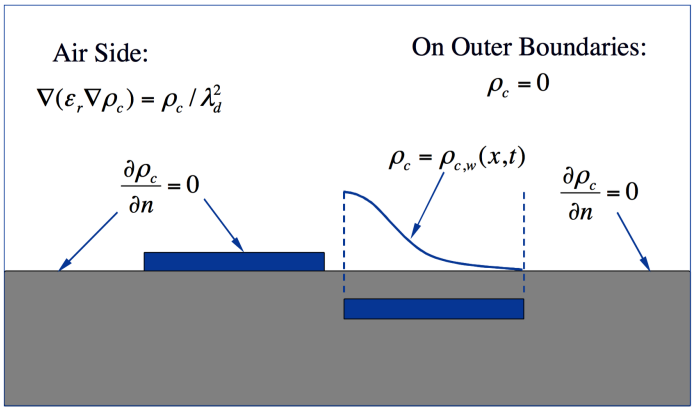

Figure 2.7: The boundary conditions used in the solution for charge density. [19]

The second potential, the potential due to the electric field, is solved for over the entire domain, not just the air side. Because the permittivity is different in the air and dielectric, equation 2.6 cannot be rewritten and must be solved as-is. At the domain boundaries, $\frac{\partial \phi}{\partial n} = 0$. For the covered electrode, $\phi = 0$ because it is the ground. The potential on the exposed electrode is set to the potential due to the input, $\phi = \phi(t)$. $\phi(t)$ is the product of the input waveform, $f(t)$, and the peak voltage, ϕ^{max}

$$\phi(t) = \phi^{max} f(t). \tag{2.13}$$

These boundary conditions are summarized in Figure 2.8.

In order to decrease the computation time required, equations 2.11 and 2.13 can be made into normalized, time-independent equations by assuming $\rho_c^{max} f(t)$ and $\phi^{max} f(t)$ both equal 1. Using these normalized boundary conditions, equations 2.10 and 2.6 can be used to solve for normalized ρ_c and ϕ fields, respectively. Once these normalized fields are known, the time-dependent fields could easily be determined by multiplying each by $\rho_c^{max} f(t)$ and $\phi^{max} f(t)$.

These two time-dependent fields are solved for at each time step in a transient flow solver. From equations 2.1 and 2.2, the body force per unit volume in terms of the two fields is:

$$\vec{f_B} = \rho_c(-\nabla\phi). \tag{2.14}$$

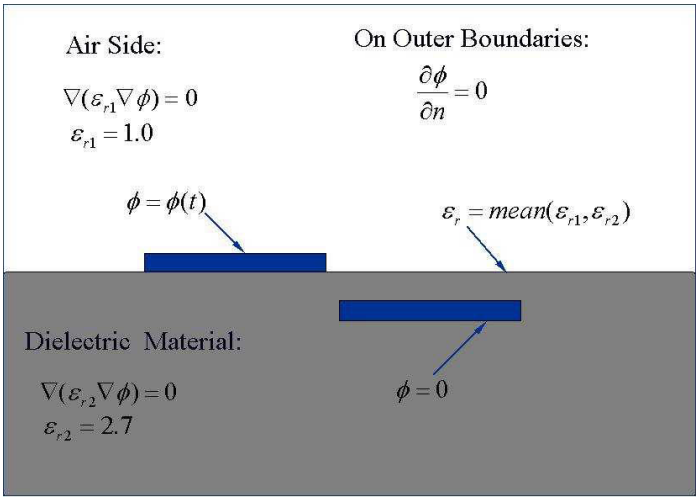

Figure 2.8: The boundary conditions used in the solution for electric potential. [19]

This body force is then used directly with a Navier-Stokes solver as a source term. Figure 2.9 shows a flow chart summarizing the steps required in the model.

The plasma actuator model was implemented in ANSYS Fluent 17.1. Fluent has an option to input user-defined functions (UDFs), which can be utilized to solve required equations for the model. Code written in C was borrowed from [20] and slightly modified to utilize this UDF feature. It is included in Appendix B. The UDF code performs four calculations: the electric field, $\vec{E}$, the source term used in the equation 2.10, $\frac{\rho_c}{\lambda_d^2}$, the x-

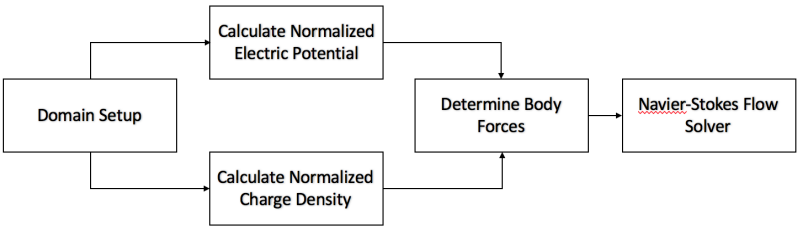

Figure 2.9: Overview of the main steps required for the Suzen model. The normalized electric potential and charge density are independent of each other, and therefore can be solved simultaneously.

and y-components of the body force, $\vec{f_b}$, and the charge density distribution on the surface above the covered electrode, $G(x)$. Fluent also features a solver for user-defined scalar (UDS) transport equations. The general form of the UDS equation includes unsteady, flux, diffusivity, and source terms:

$$\frac{\partial \phi_k}{\partial t} + \frac{\partial}{\partial x_i}\left[F_i \phi_k - \Gamma_k \frac{\partial \phi_k}{\partial x_i}\right] = S_{\phi_k}. \tag{2.15}$$

Both differential equations are steady and contain no convective term, so $\frac{\partial \phi_k}{\partial t}$ and $F_i \phi_k$ are set to zero, giving:

$$\nabla \cdot \left(\Gamma_k \nabla \phi_k\right) = -S_{\phi_k}. \tag{2.16}$$

To solve equation 2.6, the parameters are set $\phi = \phi$, $\Gamma = \varepsilon_r$, and $S_\phi = 0$. Similarly, to solve equation 2.10, the parameters are $\phi = \rho_c$, $\Gamma = \varepsilon_r$, and $S_\phi = -\frac{\rho_c}{\lambda_d^2}$. Fluent could be set to solve for both of these scalar fields in their respective domains once at the beginning of the solution.

To aid in verification, the 2D flow domain was set up to match the domain used in [19]. The domain is a square with sides of length 4 cm. In the y-direction, the domain is split in half. The top half is the air side of the domain and the bottom half is the dielectric. Both electrodes have a width of 1 cm and height of 0.0102 cm. The exposed electrode is positioned on the surface of the dielectric with the right edge at the center of the domain. The covered electrode is 0.0127 cm below the dielectric surface and is separated from the exposed electrode by a 0.005 cm horizontal gap. A mesh, shown in Figure 2.10, containing 14,792 triangular cells was created in Altair Hyperworks 14.0 and imported into the Fluent solver.

Boundary conditions on the domain were set in Fluent to match those shown in Figures 2.8 and 2.7. There is no velocity in the air other than that induced by the actuator. The two UDS equations were set as described above and a UDF was

2.2.1 Model Solution

Figures 2.11 and 2.12 compare the results presented by Suzen *et al.* to the results obtained in Fluent for the normalized electric potential and normalized charge density fields, respec-

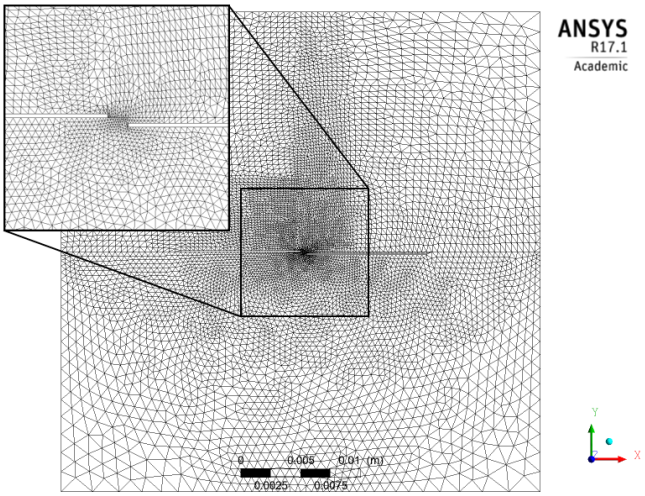

Figure 2.10: Mesh created in Altair Hyperworks 14.0.

tively. The results do not exactly match, but that is expected due to differences in grid creation and solvers used.

Once the charge density and electric potential are known, the forces on the fluid could be found using equation 2.14 over the entire domain. These forces are then applied as momentum source terms to the Navier-Stokes solver in Fluent. Figure 2.13 is a contour plot of the horizontal velocity. Figure 2.14 shows the velocity vectors calculated by Fluent. These results show a relatively large horizontal velocity component near the wall with close to no vertical components.

Figure 2.15 compares the velocity profiles at different x-locations downstream from the plasma actuator found through experiments with the velocity profiles calculated by the model. While the values are significantly different due to different actuator configurations and input parameters, the comparison shows correct behavior in the model. The peak velocity moves away from the wall and decreases in magnitude with distance downstream of the actuator.

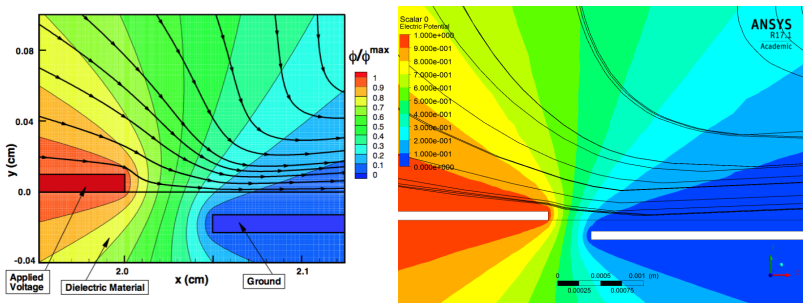

(a) Results from Suzen *et al.* [19] (b) Results obtained in Fluent.

Figure 2.11: Comparison of two solutions of the normalized electric potential contours.

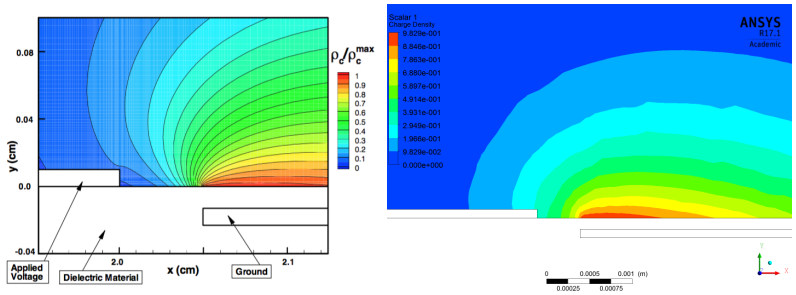

(a) Results from Suzen *et al.* [19] (b) Results obtained in Fluent.

Figure 2.12: Comparison of two solutions of the normalized charge density contours.

2.2.2 Model Discussion

While the Suzen model accurately predicts a velocity profile shape, it is not able to scale correctly with changing input voltages. It is generally accepted through experimental data that the peak velocity imparted on the flow goes approximately like $U_{max} \propto V^{7/2}$. [10] But by analyzing this Suzen model, it can be seen that the body force, f_b, is proportional to the input voltage multiplied by the maximum charge density. Because the charge density is also proportional to the input voltage, the body force calculated by the model goes like $f_b \propto V^2$. The model will under predict U_{max} with an increasing voltage.

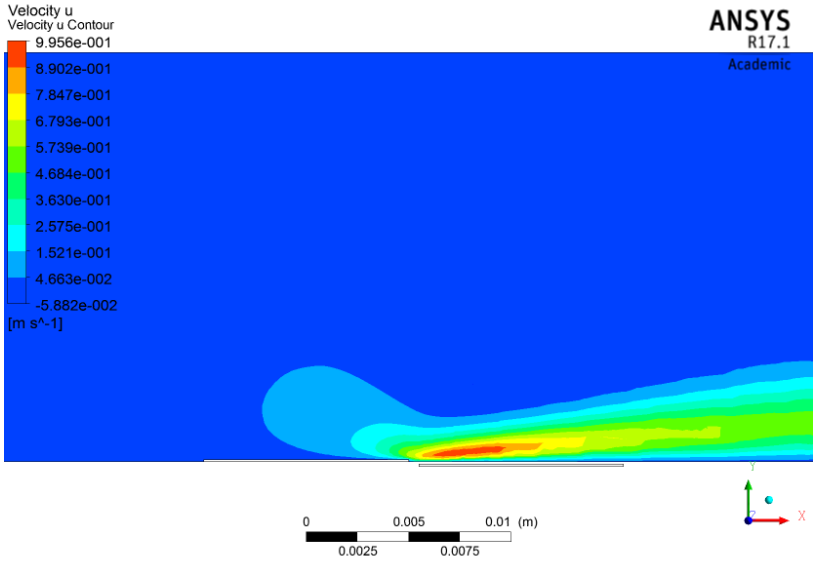

Figure 2.13: Horizonal velocity contours as calculated by Fluent.

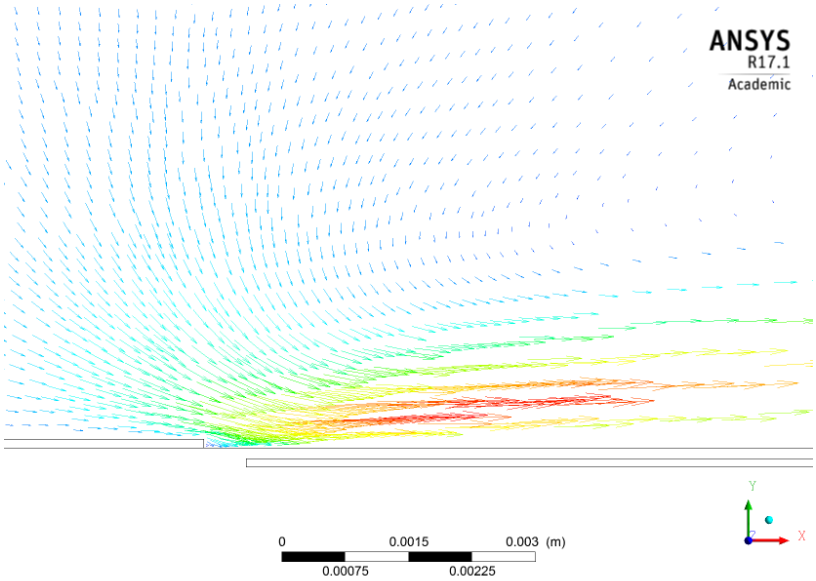

Figure 2.14: Velocity vectors as calculated by Fluent.

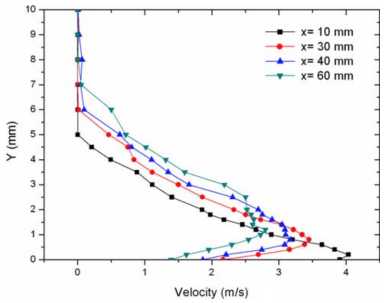

(a) Typical velocity profiles downstream of a DBD plasma actuator. [15]

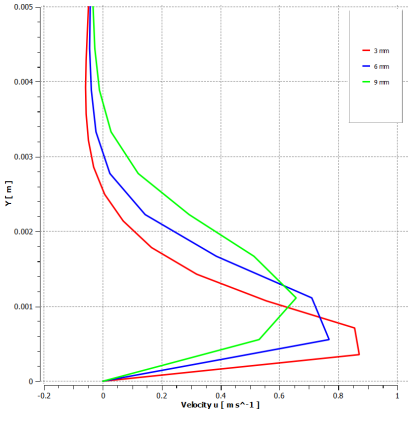

(b) Velocity profiles obtained in Fluent.

Figure 2.15: Comparison of typical velocity profiles downstream of a plasma actuator to velocity profiles obtained by the model in Fluent. The two cases are not at the same operating point, so the magnitudes should not directly be compared.

As described in [20], there are two reasons for this. Both stem from the parameters applied to the charge distribution above the encapsulated electrode. For one, the charge distribution function from equation 2.12 is constant with respect to input voltage. Experimental data has shown that with increasing voltage, the distribution of plasma over the surface, and therefore the volume of plasma, also increases. In addition to the charge distribution, the maximum charge on the surface, ρ_c^{max}, is a fixed value applied to the model. This value was chosen to tune the data to a specific input voltage and therefore does not apply to other inputs.

Each of these problems could be solved by first looking at experimental data for a specific configuration one is interested in and tuning the parameters to match the data. This could be an acceptable solution if only one specific geometry at one specific operating condition will be considered. A more robust model could be created by modeling these parameters as functions of the input voltage. The electric circuit plasma actuator model, as described in [13], [11] is one such attempt. This model uses a series of N sub-circuits spaced

over the length of the encapsulated electrode. Each sub-circuit contains the resistivity and capacitance of air and the capacitance of the dielectric over a volume element. This allows for a voltage-dependent plasma distribution to be developed that is more accurately predictive of U_{max}.

2.3 Experimental Test

Due to availability of a power supply, initial experimental tests were performed using ns-DBD plasma actuators. An Eagle Harbor NSP-120-20-F was used to power the actuators. This power supply provide high voltage pulsed signals with maximum properties of a 500 ns pulse width, 10 kHz pulse frequency, and 20 kV peak voltage. The pulser is limited by an operating envelope, so these maximums could not all be achieved simultaneously.

A series of tests were performed to determine first if the power supply is capable of powering actuators and also to determine roughly what parameters worked best to create the plasma. A series of 2.5" long by 0.25" wide strips of copper tape were applied to a polycarbonate plate. The electrode gap in all cases was roughly 0.1". Kapton tape with a thickness of 1 mil was used as the dielectric. The thickness of the Kapton was varied by adding strips of tape. The thickness varied from one strip (1 mil) to four strips (4 mil). In addition to tests with one actuator, tests with two and three actuators in parallel were performed.

Each test was performed at a pulse frequency of 100 Hz and began with a pulse width of 250 ns. The voltage was incrementally increased until the first signs of plasma were observed to determine the minimum voltage required to create plasma for each configuration. The voltage was then increased again until the plasma burned through the Kapton or otherwise shorted the circuit. If the maximum output voltage of 20 kV was reached, the pulse width was then increased incrementally with voltage until a maximum operating point was reached. With four strips of Kapton, no maximum was found over the entire operating envelope of the power supply. The results of these test are summarized in Table 2.1. Repeatability was difficult to achieve because the maximum voltage achievable is very sensitive to variations in geometry. Each time an actuator was burned through, a new one would have to be made. Any irregularity, such as an air bubble under the tape or a sharp corner of an electrode,

can cause the actuator to fail early.

Table 2.1: Results from the test of an ns-DBD plasma actuator to determine a geometry that would consistently produce plasma.

Strips of Kapton	Frequency (Hz)	V_{min} (kV)	V_{break} (kV)	Pulse Width (ns)
1	100	8.6	11	250
2	100	8.0	18	400
3	100	9.4	20	250
4	100	9.6	–	–

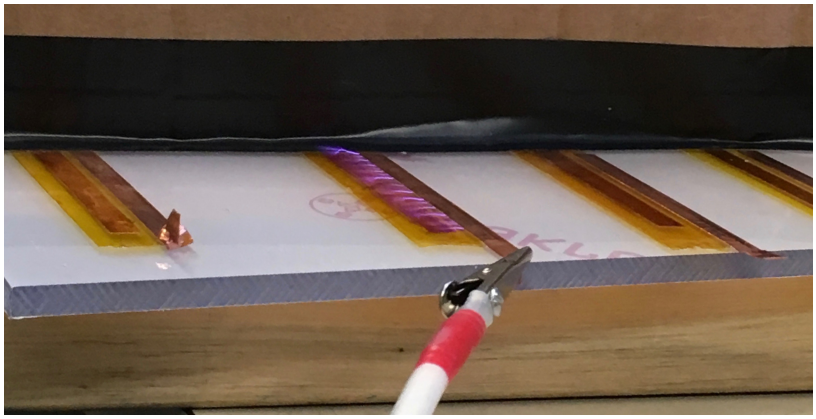

Figure 2.16: Plasma formation between two electrodes during testing.

Chapter 3

VORTEX DETECTION

3.1 Background

3.1.1 Coefficient of Pressure Profile Derivation

Below a vortex, the velocity along the surface will be a sum of the freestream velocity and the velocity induced by the vortex. Therefore, the pressure below a vortex decreases with a minimum directly below the center. The circulation around a closed curve is defined by the integral

$$\Gamma = \oint_c \vec{v} \cdot d\vec{l}. \tag{3.1}$$

In the case of a two-dimensional vortex represented as a circle, as shown in Figure 3.1, the integral can be converted to

$$\Gamma = \int_0^{2\pi} v_\theta r d\theta = 2\pi v_\theta r, \tag{3.2}$$

with v_θ being the magnitude of the tangential velocity and r being the distance from the center of the circle. The tangential speed represented as a function of Γ and r is

$$v_\theta = \frac{\Gamma}{2\pi r}. \tag{3.3}$$

In the method of images, a flat surface near a vortex is represented by an image vortex that is a mirror reflection across the surface of the real vortex, as shown in Figure 3.1. The z-component of velocity contributed by just the real vortex at any point along that surface is

$$v_z(z) = v_\theta \cos\theta = \frac{\Gamma h}{2\pi(h^2 + z^2)}. \tag{3.4}$$

When the image vortex is included, the velocity parallel to the surface becomes $2v_z$. The y-components of velocity provided by the two identical vortices cancel. This leaves the velocity along the wall to be $\vec{w} = 2\vec{v}_z$. From equation 3.4, the magnitude w as a function

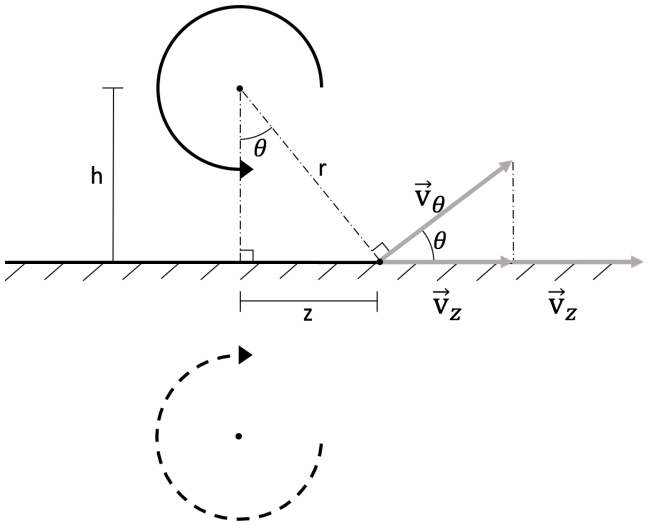

Figure 3.1: Diagram of a vortex and its image including relevant dimensions as labeled.

of z becomes

$$w(z) = \frac{\Gamma h}{\pi(h^2 + z^2)}. \tag{3.5}$$

For a potential flow, the pressure coefficient can be represented by

$$C_p = \frac{p - p_\infty}{\frac{1}{2}\rho U_\infty^2} = 1 - \left(\frac{u}{U_\infty}\right)^2, \tag{3.6}$$

where u is the local velocity. In this case, the local velocity is the sum of the orthogonal velocity vectors, $\vec{w}$ and the freestream velocity, $\vec{U}_\infty$.

$$C_p(z) = 1 - \frac{w^2 + U_\infty^2}{U_\infty^2}. \tag{3.7}$$

Substitution and simplification yields the final form:

$$C_p(z) = -\left[\frac{\Gamma h}{\pi(h^2 + z^2)U_\infty}\right]^2. \tag{3.8}$$

3.1.2 Vortex Drift Derivation

Vortices formed by vortex generators propagate at a slight angle off the direction of U_∞. This angle can be determined by finding the velocity imparted on the vortex by its image.

As with before, the tangential velocity at any point a distance r from the center of a vortex is given by equation 3.3. The center of the real vortex is located a distance of $2h$ from the center of its image. Therefore, the image vortex imparts a drift velocity of magnitude

$$v_{drift} = \frac{\Gamma}{4\pi h}. \tag{3.9}$$

The angle at which the vortex propagates away from the freestream, α, is the inverse tangent of v_{drift}/U_∞, or

$$\alpha = \tan^{-1}\left(\frac{\Gamma}{4\pi h U_\infty}\right). \tag{3.10}$$

3.2 Experimental Setup

Two wind tunnel tests were performed in the Kirsten Wind Tunnel (KWT) at the University of Washington Aeronautics Lab (UWAL). The KWT is subsonic, closed, double return wind tunnel with a test section $8'$ tall by $12'$ wide and is $10'$ long. It is capable of generating flow up to 100 psf, which correspond to roughly 200 mph. The tunnel facility also has the capability of producing smoke for flow visualization purposes.

Two Scanivalve ZOC33/64Px electronic pressure scanning modules were used to measure the pressure on the surface of the plate. Each scanner contains 64 piezoresistive pressure sensors, for a total of 128. The scanners are capable of measuring up to ± 5 psi differential with an accuracy of $\pm 0.08\%$ full scale (± 0.004 psid). The temperature sensitivity is 0.10% full scale/°C. The 64 sensors are contained internally in a module. Vinyl tubing is run from the ports on the module to adapters which are inserted in holes in the plate.

A 3/16" thick aluminum plate was cut to 26"x30" to be used in the experiment. An array of 1/8" diameter holes was milled in the plate for installation of the adaptors for the pressure scanners. This array contained 36x16 holes with spacing of 0.4" and 1", respectively. The large array of 576 holes was made to allow for flexibility when positioning the adaptors. Upstream of the array, more holes were milled to provide mounting locations for the vortex generators. Each mounting location was made up of four holes to allow the vortex generator to be positioned at angles of 15°, 20°, and 25°. The leading edge of the plate was rounded to reduce any flow separation upstream of the vortex generators. Figure 3.2 provides a dimensioned drawing of the plate.

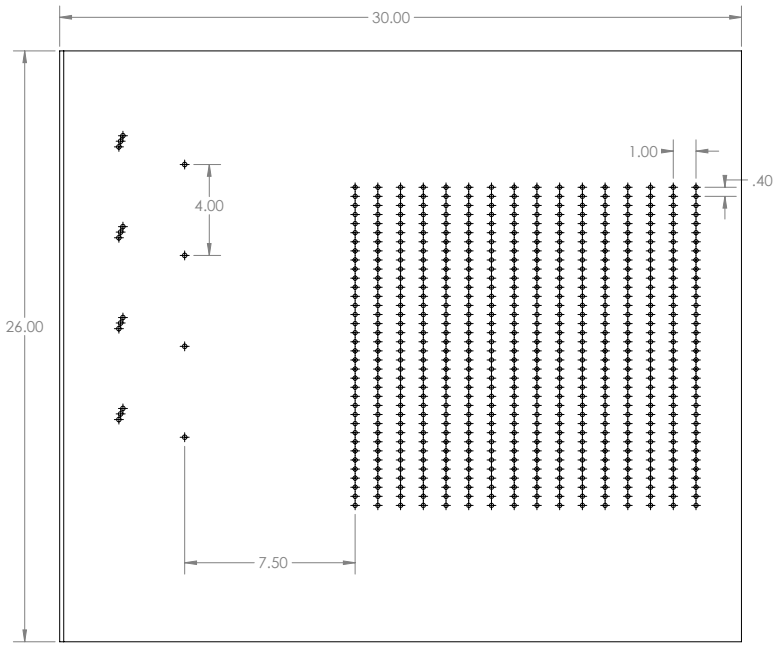

Figure 3.2: Dimensioned drawing of the plate used in the wind tunnel experiments. All dimensions are in inches. The plate had a thickness of 3/16".

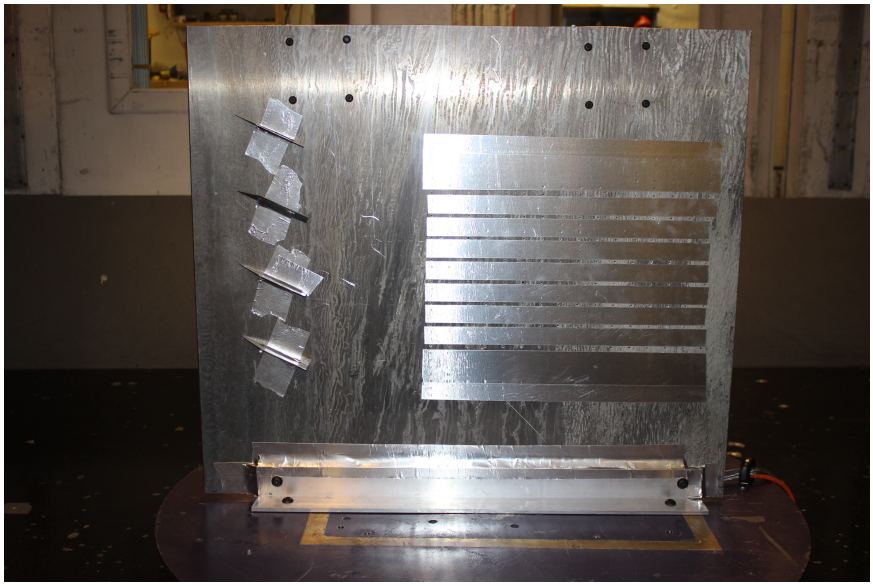

Figure 3.3: Image of the plate mounted in the wind tunnel with four vortex generators at an angle of 25°.

The plate was mounted vertically on a turntable on the floor of the KWT. The turntable gave the option to place the plate at precise angles of attack. Figure 3.3 shows the plate mounted in the tunnel in a four vortex generator configuration. For every run, the plate was angled at $-2°$. Only 128 pressure channels were available, so pressure data could not be read at all 576 milled locations simultaneously. The rows shown in Figure 3.4a were chosen for this initial test to capture the entire pressure footprint from the middle two vortices while retaining a fairly dense grouping of data points. The spacing used was 1.2" in y and 1" in x. Vane-type vortex generators were used with a height of 1", chord length of 4", and thickness of 1/32". The leading edge angle of the vortex generators was 35 degrees.

The first run was performed with no vortex generators, or a "clean" plate. The tunnel wind speed is monitored by measuring the dynamic pressure, q. The wind speed can then be calculated using tunnel density, temperature, and pressure measurements. Beginning with the wind off (0Q), data were recorded in increments of roughly $q = 10\ lb/ft^2$ (10Q) until the setup appeared unstable. For the steady plate, this was 70Q. Therefore, 70Q became

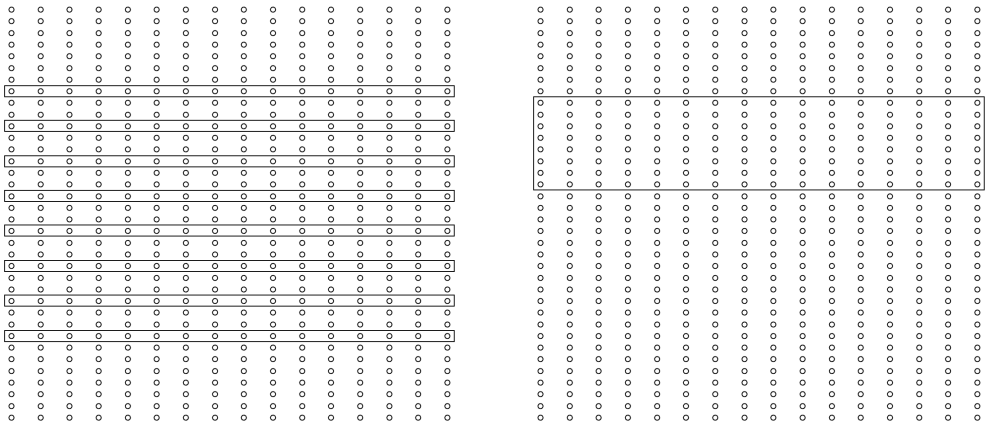

(a) First test. (b) Second test.

Figure 3.4: Graphic showing the rows used to position sensors for the two wind tunnel tests.

the max dynamic pressure tested. The data include the exact tunnel dynamic pressure at each nominal value, the measured temperature and static pressure values of the tunnel, and the differential pressure measured for each of the 128 scanners. The pressure recorded by the scanners was an average over a ten second range to remove any unsteady effects. Subsequent runs with various configurations of vortex generators were run until either the 70Q was reached, or a vortex generator deflected and appeared likely to break off. Two runs were performed with smoke flow visualization to provide a visual confirmation of the vortex locations.

A second wind tunnel test was performed with decreased spanwise pressure sensor spacing. The 1.2" spacing was decreased to 0.4" with only a single vortex tested for each case. This configuration is shown in Figure 3.4b. Clean plate data was first recorded, followed by one run to 70Q at the three vortex generator angles. The final run introduced a plasma actuator downstream of the vortex generator. Data was recorded with the actuator both on and off at 30Q, 40Q, and 50Q. The two tests are summarized in Table 3.1. Figure 3.5 shows an example of the flow visualization used.

Table 3.1: Summary of the runs completed for both wind tunnel tests.

Test #	Run #	# of VGs	VG Angle	Max Q (psf)	Notes
1	1	0	N/A	70	–
1	2	4	15°	70	–
1	3	4	20°	60	–
1	4	4	25°	40	–
1	5	4	15°	30	Smoke
1	6	1	15°	50	Smoke
2	1	0	N/A	70	–
2	2	1	15°	70	–
2	3	1	20°	70	–
2	4	1	25°	70	–
2	5	1	15°	50	Plasma

3.3 Wind Tunnel Data Analysis

Rather than the differential pressure values measured, all data analysis was done using the dimensionless pressure coefficient, C_p. The software used in the wind tunnel automatically determined these values by dividing the differential pressure by the dynamic pressure. The lengths were also normalized with respect to the 1" height of the vortex generators. Runs below 40Q were not considered in the analysis due to the significance of the error for those runs. As mentioned, the Scanivalve units used are accurate to $\pm 0.004 psid$. This error creates an uncertainty of roughly 40% in the peak differential pressure under a vortex at low speeds. Even at the higher wind speeds, visual inspection of a surface plot of the data showed multiple data points which were obvious outliers. These were mostly caused by insufficient seals at some point in the pressure connections. Some outliers were consistent through all runs, whereas some appeared midway through the testing. The vertical column of pressure sensors nearest the vortex generators had multiple outliers, so it was determined

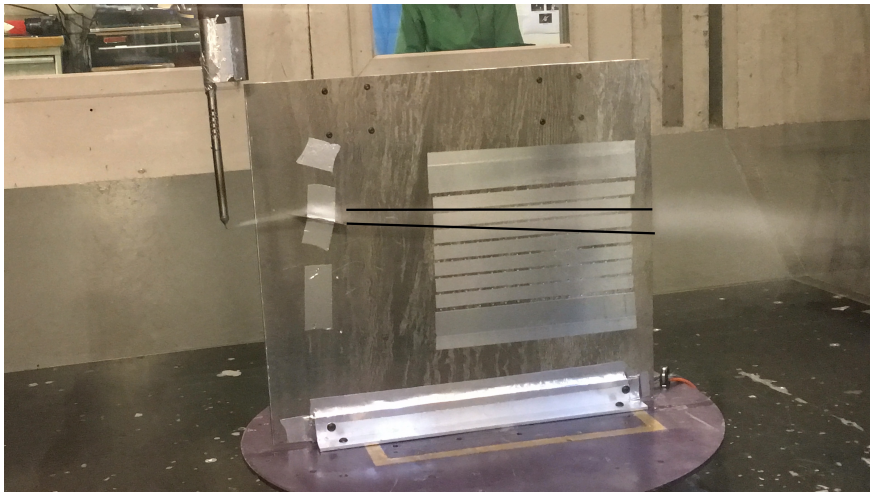

Figure 3.5: Smoke flow visualization for the case with one vortex generator at 15°.

that ignoring this column altogether was the best way to proceed. After this column was ignored, only two outliers remained. To be consistent, these measure values were replaced with linearly interpolated values for all runs, even in cases where the data appeared to be accurate. Figure 3.6 shows a comparison of the raw data with different corrections applied.

Even with the clean data, as in Figure 3.6c, it is difficult to determine the location of the vortices from the raw data. The overall pressure changes across the plate due to the $-2°$ angle of attack are larger than the slight pressure changes expected beneath a vortex. Rather than looking at the raw C_p values, it is better to look at the difference between the C_p values found from the clean plate test and the C_p values for each run. Figure 3.7 compares the raw data with the differential C_p for cases with one and four vortex generators. The paths of the vortices can be clearly seen in both the surface and the linearly interpolated pseudocolor plots.

The plot of a single y-column of pressure sensors in Figure 3.7c is shown in Figure 3.8. This plot does not provide the exact location of the vortex center because the sensor spacing is relatively large. Just by inspection, it can be determined that the center is somewhere between $y = 2$ and $y = 3$. To get a more accurate solution, six curve fits and one equation

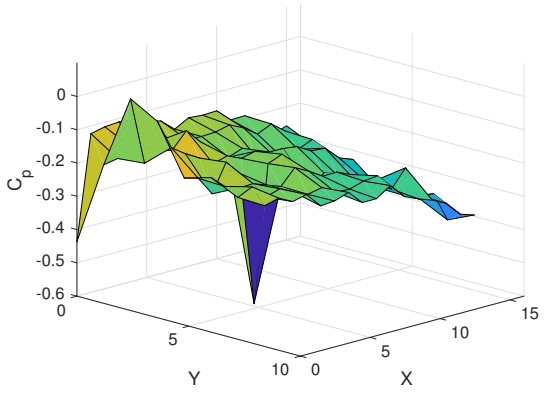

(a)

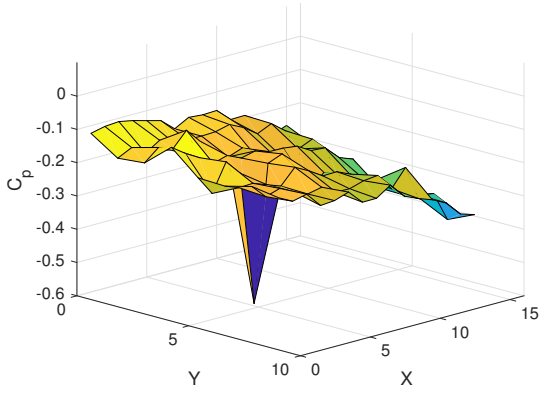

(b)

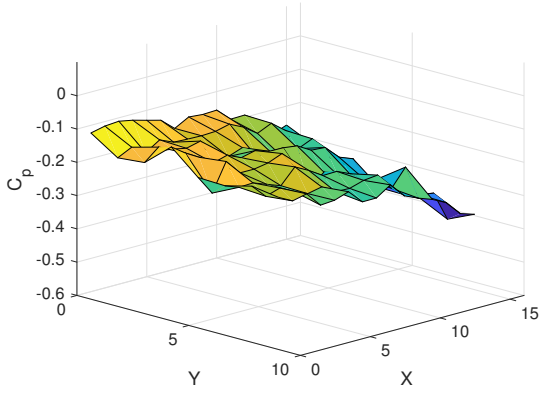

(c)

Figure 3.6: Surface plots showing (a) the raw coefficient of pressure data for a particular run, (b) the data after the first row is removed, and (c) the data with all outliers removed.

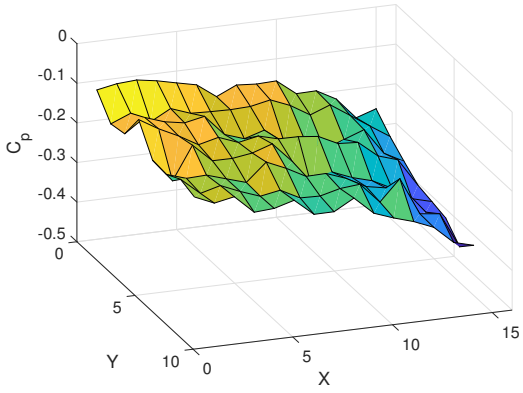

(a) One VG – Raw C_p data

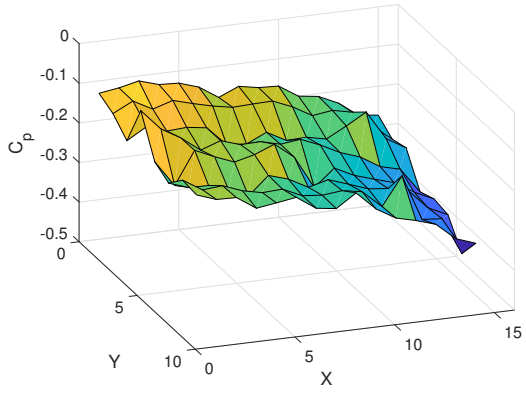

(d) Four VGs – Raw C_p data

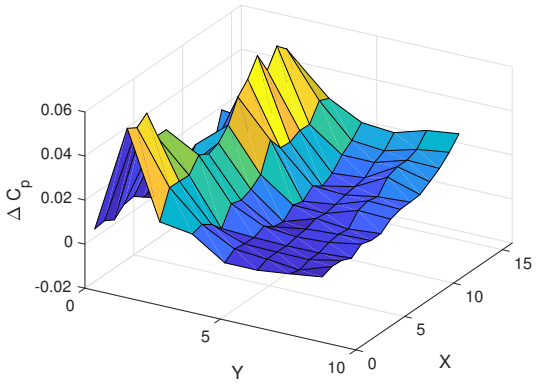

(b) One VG – ΔC_p

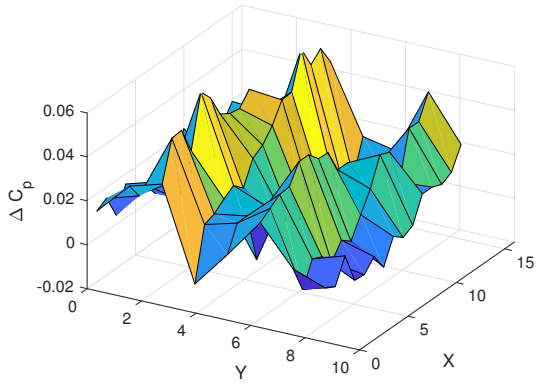

(e) Four VGs – ΔC_p

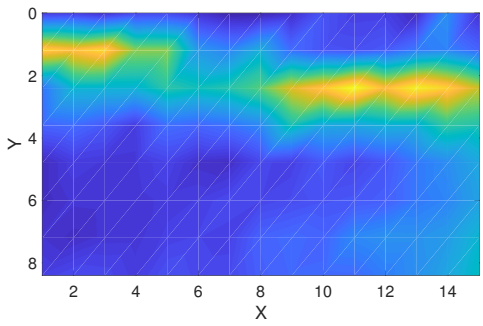

(c) One VG – ΔC_p

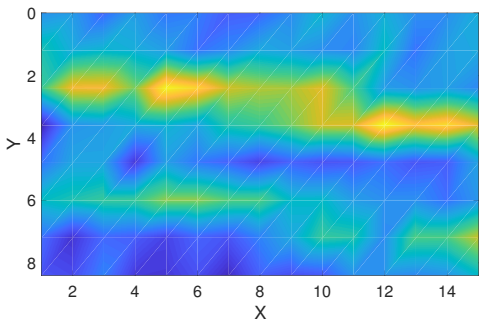

(f) Four VGs – ΔC_p

Figure 3.7: Comparison of raw C_p data for runs of one and four vortex generators with the differential C_p data for the same runs.

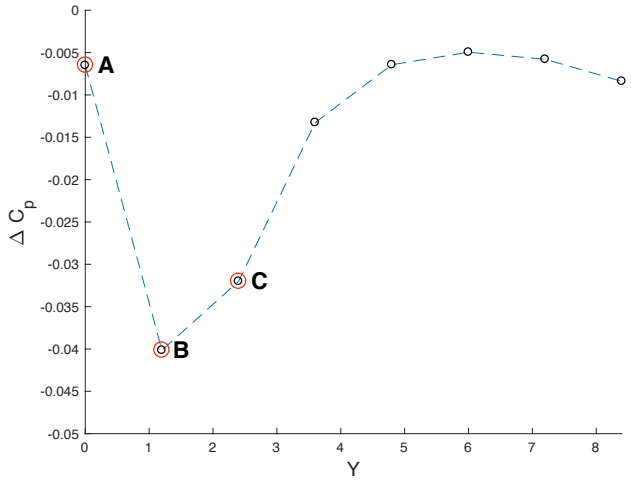

Figure 3.8: Differential C_p for a single column of pressure sensors in the one vortex generator case. The data points used in the three point fits are circled in red.

were compared. Four fits used all eight data points in the column. The other three used just the largest value measured and the two data points adjacent to it. These three points are circled in red in Figure 3.8.

The four fits using all eight data points were curve fits to the theoretical pressure distribution described earlier by equation 3.8. The unknown values in this equation are Γ and h. The height of the vortex is expected to be roughly 0.8 times the height of the vortex generator. So the first fit sets $h = 0.8$. The second fit allows Matlab to choose a value for h that best fits the data, even though it may be wrong. The third and fourth fits are the same as the first two, but attempt to correct for the C_p offset observed in Figure 3.8. Theoretically, the plotted differential C_p should be zero everywhere besides under the vortex. But, as seen in the figure, there is an offset far from the vortex. This offset had a fairly consistent value of roughly 0.01 throughout the data. The second and third fits therefore add another unknown, $C_{p-offset}$, to fit the curve to the offset rather than to zero.

The last three methods utilize just three pressure sensors. The first of these again fits to the curve given by equation 3.8 while allowing h to vary. The second introduces the

$C_{p-offset}$ term with a set value of $h = 0.8$. The third finds a center by comparing the ratio, R, of the difference the peak and the middle point and the peak and the lowest point. If the points are labeled from left to right, A, B, and C, as they are in Figure 3.8, and the spacing between the sensors is d, the formula is as follows:

$$y_{center} = y_B + \frac{d}{2} R^2 \left[\frac{C_{pA} - C_{pC}}{|C_{pA} - C_{pC}|} \right], \tag{3.11}$$

where

$$R = \frac{C_{pB} - min[C_{pA}, C_{pC}]}{C_{pB} - max[C_{pA}, C_{pC}]}. \tag{3.12}$$

The center will always fall within a range of $\pm\frac{d}{2}$ from the location of the peak data point. The equation therefore uses the ratio to determine a center location in the range $-\frac{d}{2} < y_{center} < \frac{d}{2}$.

Figure 3.9 compares the six fits used for one particular set of data. The center from equation 3.11 is omitted because it just finds a center rather than creates a fit. The curves of the six fits are dramatically different, with varying heights and widths. But, the location of the center, represented by the $*$, remains relatively the same. These fits would therefore not be useful in determining Γ or h, the variables that affect the shape of the curve, but may still be able to consistently find the location of the vortex.

Figure 3.10 compares the results of finding the centers with all seven methods for a specific run. It immediately stands out that the centers found with all seven methods are fairly consistent for most columns of sensors. The percent difference between each center location and the average for that column is shown in Figure 3.11. The average percent difference for each method over all runs was calculated and shown in Table 3.2. Equation 3.11 yields the lowest average percent difference, followed by the fits with the C_p offset, and lastly the fits with no offset. Based on these percent differences alone, there is no real advantage to using all eight sensors rather than three. Examination of Figures 3.10 and 3.11 reveals that besides the single outlier at the end, the grouping is generally very consistent when the vortex is between two sensors. But, as it passes over a row of sensors, the fit methods seem to have a hard time accurately fitting the data and the grouping of center locations spreads out significantly.

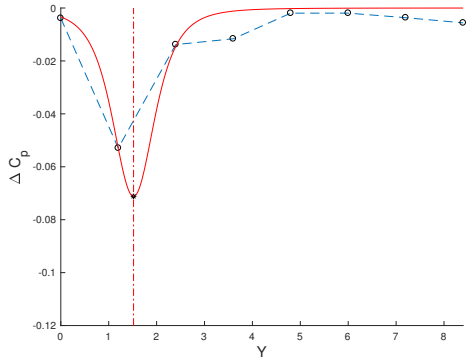

(a) Full Fit – h=0.8

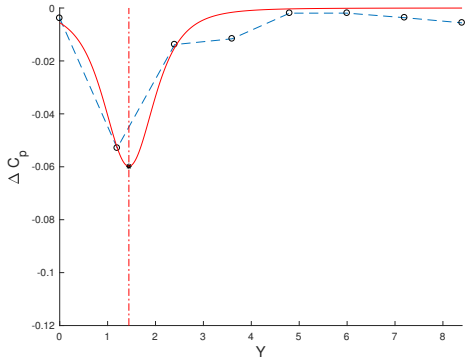

(b) Full Fit – h=variable

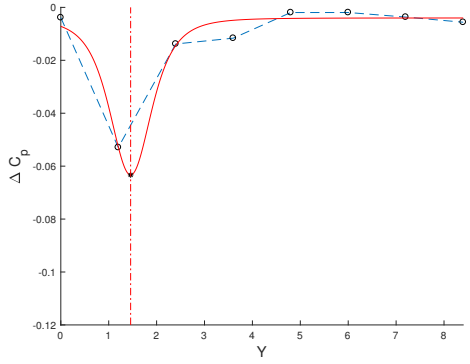

(c) Full Fit + y-offset – h=0.8

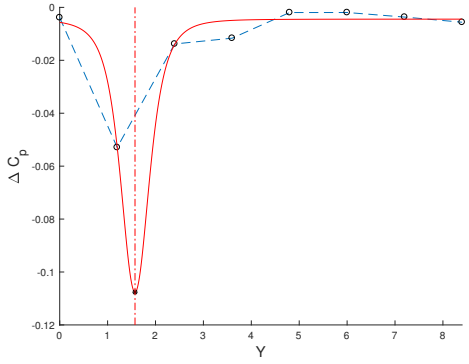

(d) Full Fit + y-offset – h=variable

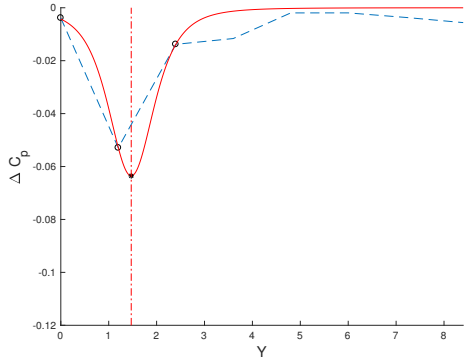

(e) 3 Sensor Fit – h=variable

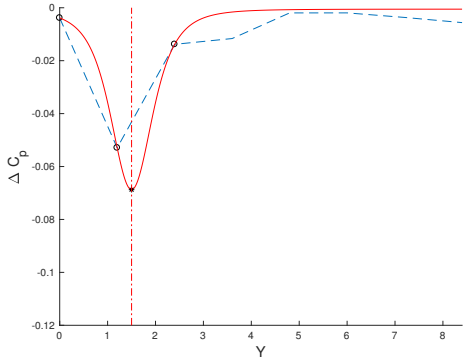

(f) 3 Sensor Fit + y-offset – h=0.8

Figure 3.9: Comparison of the six different fits used for the same set of data. The data is shown by the dashed line, with the points being utilized for that specific fit as circles. The center found at the ΔC_p peak is represented by the $*$.

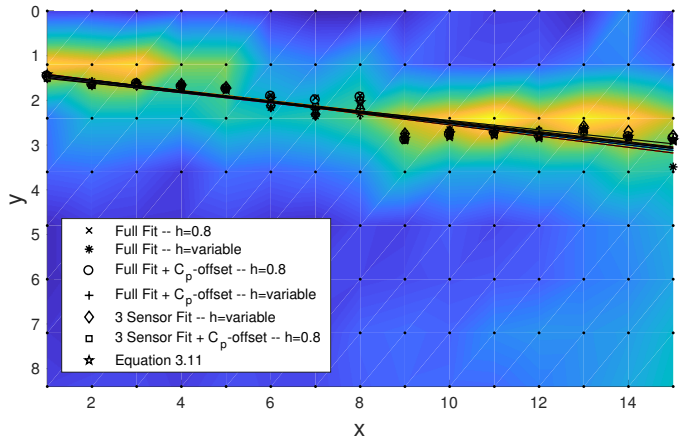

Figure 3.10: Linearly interpolated pseudocolor plot of ΔC_p with an overlay of the center locations determined by each fit for Test 1, Run 5 at $q = 40lb/ft^2$.

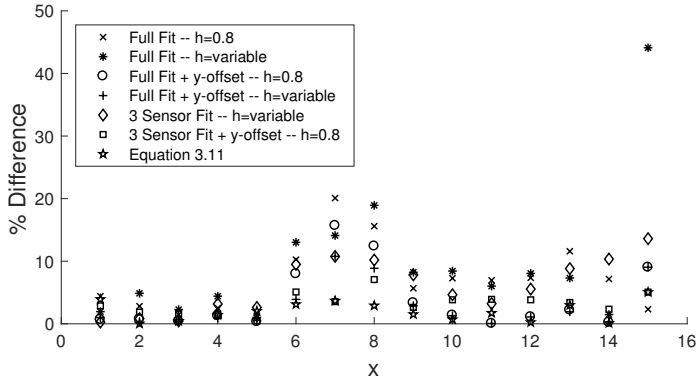

Figure 3.11: Percent differences normalized by spanwise sensor spacing between each center and the average of each for Test 1, Run 5.

Table 3.2: Percent difference and the coefficient of determination, R^2, for the seven methods used to find the center of a single vortex for Test 1.

Symbol	Method	Offset?	h	Percent Difference	R^2
$\times$	Full Fit	No	0.8	7.25%	0.8445
$*$	Full Fit	No	variable	10.49%	0.9118
$\circ$	Full Fit	Yes	0.8	3.54%	0.8567
$+$	Full Fit	Yes	variable	2.50%	0.8773
$\diamond$	3 Sensor Fit	No	variable	6.54%	0.8748
$\square$	3 Sensor Fit	Yes	0.8	3.38%	0.8700
$\star$	Equation 3.11	N/A	N/A	2.06%	0.8832

The same analysis was repeated for the cases with multiple vortices. It would not make sense to use the fit methods that used eight sensors here because there are two vortices over the width of the sensor array. Therefore, this analysis is limited to just the three three-sensor methods. Figure 3.12 compares the two three-sensor fits with and without an offset at one spanwise location. The centers found by each method and their percent difference from the average are shown in Figures 3.13 and 3.14. The averages of these percent differences are summarized in Table 3.3. The results shown are consistent with the results from the one vortex generator case above. Equation 3.11 provided a center location the most consistent with the averages of each method. In this case, the inconsistent grouping where the vortex passes over a pressure sensor does not show up, most likely due to the only three-sensor methods being used and the differences with how these fits work compared to the eight-sensor fits.

The second test was done to determine how the sensor spacing affected the data and curve fits. As previously mentioned, the spanwise spacing was reduced to 0.4" while the streamwise spacing remained 1". Figures 3.15 and 3.16 show the resolved locations of the centers and the percent differences. Table 3.4 gives the mean percent differences for each method over all runs. These percent differences were found to be slightly higher than those

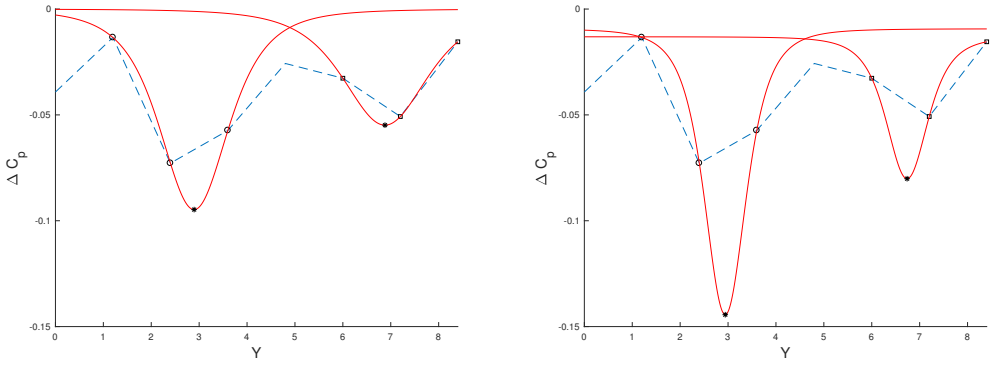

(a) 3 Sensor Fit – h=0.8 (b) 3 Sensor Fit + C_p offset – h=variable

Figure 3.12: Comparison of two fits used to find the center when two vortices are present over the pressure sensor array.

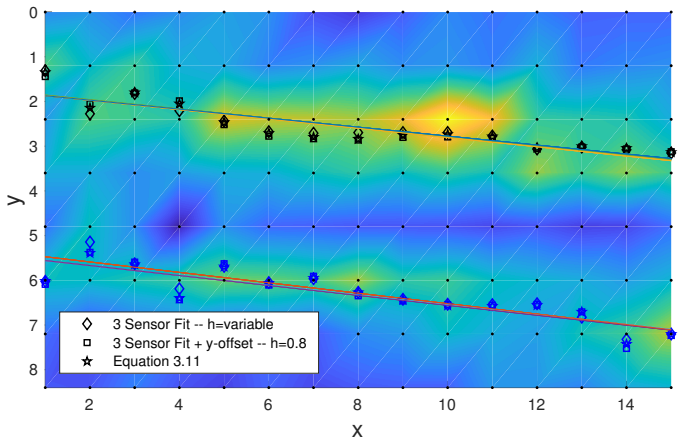

Figure 3.13: Linearly interpolated pseudocolor plot of ΔC_p with an overlay of the center locations determined by each fit for Test 1, Run 2 at $q = 40lb/ft^2$.

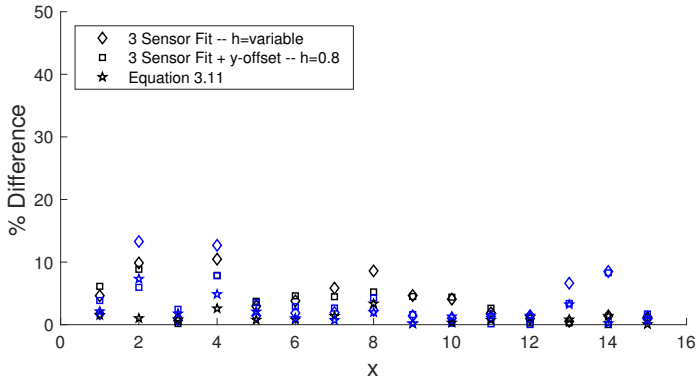

Figure 3.14: Percent differences normalized by spanwise sensor spacing between each center and the average of each for Test 1, Run 2.

found in the first test with 1.2" spanwise spacing. But, the percentages are all normalized by the sensor spacing. Therefore, the 0.4" spacing provides an absolute accuracy that is slightly less than three times that of the 1.2" case due to the closer grouping of sensors.

3.4 Test with Plasma Actuator

To test the influence of an ns-DBD plasma actuator on a vortex, one was placed roughly four inches downstream of a vortex generator angled at 15° so that the vortex would pass roughly through the center of the actuator. The plasma actuator was one inch long and had a gap spacing of 0.1". It was oriented so that the induced momentum was in the same direction of the azimuthal velocity of the vortex at the surface. "Safe" parameters based on the results from section 2.3 above were chosen to prevent any burn through of the actuator that would cause the test to be aborted and restarted. Two layers of Kapton tape were used with power supply parameters of 250 ns pulse width, 100 Hz frequency, and 14 kV peak voltage. The plate and plasma actuator mounted in the wind tunnel is shown in Figure

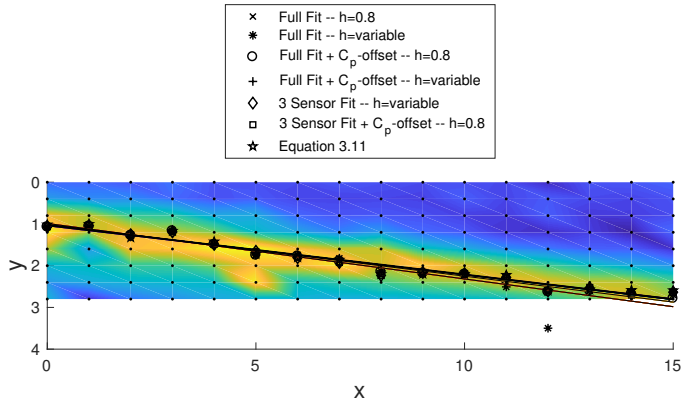

Figure 3.15: Linearly interpolated pseudocolor plot of ΔC_p with an overlay of the center locations determined by each fit for Test 2, Run 2 at $q = 40lb/ft^2$.

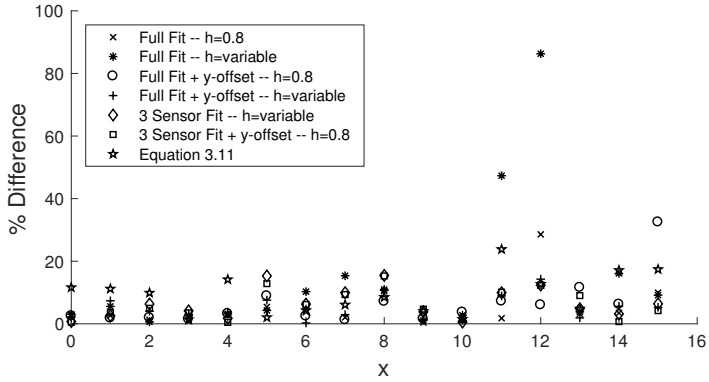

Figure 3.16: Percent differences normalized by spanwise sensor spacing between each center and the average of each for Test 2, Run 2.

Table 3.3: Percent difference and the coefficient of determination, R^2, for the three methods used to find the center of two vortices for Test 1.

Symbol	Method	Offset?	h	Percent Difference	R^2
$\diamond$	3 Sensor Fit	No	variable	3.84%	0.8707
$\square$	3 Sensor Fit	Yes	0.8	4.23%	0.8491
$\star$	Equation 3.11	N/A	N/A	2.47%	0.8678

Table 3.4: Percent difference and the coefficient of determination, R^2, for the seven methods used to find the center of a single vortex for Test 2.

Symbol	Method	Offset?	h	Percent Difference	R^2
$\times$	Full Fit	No	0.8	11.43%	0.9797
$*$	Full Fit	No	variable	7.07%	0.9556
$\circ$	Full Fit	Yes	0.8	7.75%	0.9817
$+$	Full Fit	Yes	variable	8.90%	0.9817
$\diamond$	3 Sensor Fit	No	variable	7.86%	0.9674
$\square$	3 Sensor Fit	Yes	0.8	8.03%	0.9745
$\star$	Equation 3.11	N/A	N/A	22.16%	0.7989

3.17. The wind tunnel run consisted of six data points. Data was recorded at three dynamic pressures, 30Q, 40Q, and 50Q, with the plasma actuator turned off and on.

To determine if the actuator had any affect on the flow, a differential pressure coefficient was once again examined. Rather than the difference between a specific run and the clean plate case, this time the differential pressure coefficient was between consecutive cases with the actuator on and off at the same test point. Any change in the flow should result in non-zero values of ΔC_p.

Figure 3.18 plots the differential pressure coefficient with the actuator on and off. At every location measured where y is greater than 1.5, Δ_p is roughly zero, which would indicate

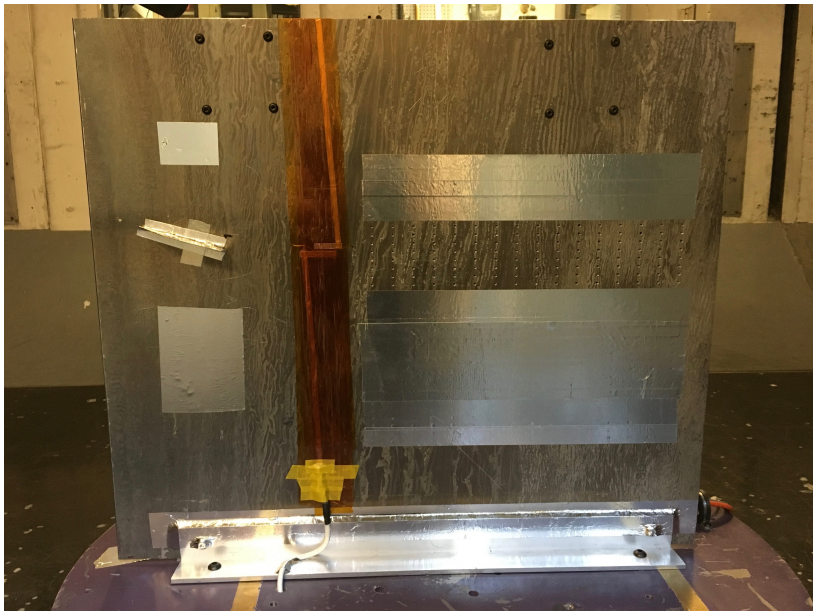

Figure 3.17: The plate with a plasma actuator applied mounted in the wind tunnel.

no change in the flow. For y values less than 1.5, there is a small but consistent positive differential pressure coefficient. This would seem to indicate a higher pressure, and therefore lower velocity, at those locations when the plasma actuator is turned on. Similar results were observed in the data taken at 30Q and 40Q. These plots are presented in Figure 3.19.

While the positive pressure difference appears fairly consistent in all three cases, the value is very small. At 30Q, the ΔC_p over the 64 pressure sensors where $y < 1.2$ is roughly 1.5×10^{-2}. As the dynamic pressure is increased, the difference becomes even smaller. At 40Q and 50Q, it decreases to 4.0×10^{-3} and 2.0×10^{-3}, respectively. The differential pressures corresponding to these are roughly 3×10^{-3}, 1×10^{-3}, and 7×10^{-4} psid. These values all fall within the error range of 0.004 psid reported for the Scanivalve sensors used.

A few locations of this small differential pressure alone would most likely be attributed to error. But, the fairly consistent values for each run and the consistent locations over the three runs would suggest the perceived difference is in fact a consequence of the the plasma actuator. Further supporting this is the fact that the pressure difference decreases as they wind tunnel velocity increases. Because the strength of the actuator remains the same for

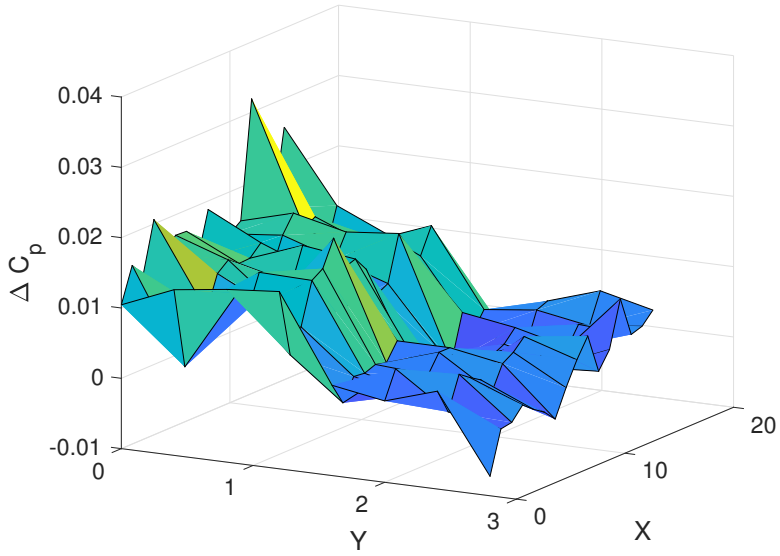

Figure 3.18: Differential C_p between consecutive runs with the plasma actuator on and off with the tunnel dynamic pressure at $30lb/ft^2$.

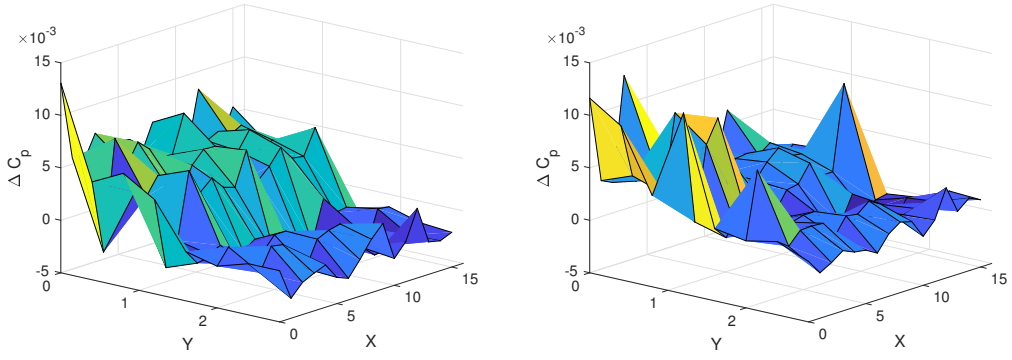

(a) (b)

Figure 3.19: Differential C_p between consecutive runs with the plasma actuator on and off with the tunnel dynamic pressure at (a) $40lb/ft^2$ and (b) $50lb/ft^2$. The $50lb/ft^2$ case introduces considerable noise compared to the magnitude of tjhe data, but a pressure increase is still observed.

all three cases, it is expected to have less of an impact on the flow.

For these tests, the plasma actuator was oriented in a way in which the induced flow is in the same direction as the vortex rotation at the surface. The expected result would be for the actuator to either move the vortex in the positive y-direction or to strengthen the vortex. The area of increased pressure is consistent with the theory that the vortex would move. But if this were the case, an area of decreased pressure would also be expected. The area of no change does not fit with the expected results. Therefore, the effect of adding the actuator is inconclusive.

Chapter 4

CONCLUSIONS

4.1 Plasma Actuators

The ideal type of plasma actuator for flow control is the dielectric barrier discharge actuator. The DBD plasma actuator induces stronger flow in a more preferable location than the corona discharge actuator. As discussed, the Suzen model of an ac-DBD plasma actuator produces inaccurate results for all cases besides a specific operating point. Using the model for a true parametric study of an ac-DBD plasma actuator would require the model to be further altered.

As summarized in Table 2.1, the Eagle Harbor nanosecond pulser used was able to create plasma over a large range of inputs. Even at the conservative operating point used during the wind tunnel test, a measurable effect on the pressure was detected downstream of the actuator by the pressure sensor array. The change in pressures shows a rise in pressure "above" the actuator and no change "below" it. The increase in pressure would be consistent with the vortex being moved in the direction of the actuator. But, the region of no change does not fit with this theory.

4.2 Vortex Detection

Based on the results presented in Tables 3.2, 3.3, and 3.4, just three sensors can be adequate to locate the center of a vortex at a spanwise location downstream of a vortex generator. The percent difference between the average location found for all fits and the three sensor fits is roughly the same if not better than that for the eight sensor fits. This is likely due to the fact that introducing more pressure data into the curve fit far from the center of the vortex increases the chance for error that will alter the fit. In the limited data that were studied, no one fit stands out as performing the best, but it appears that the fits that included the ΔC_p offset term are generally the most consistent.

When the spanwise spacing of pressure sensors is 1.2", greater than the height of the vortex generator, the curves fit to equation 3.8 are not an effective technique for finding the center. Equation 3.11 proves to be more consistent in locating the center than all seven fits used. It also correlates just as well with a linear least regression line as the six fits, which, assuming the vortex path is also linear, would seem to indicate it works just as well at finding the centers.

When the spacing is decreased to 0.4", less than half the height of the vortex generator, the seven fits perform significantly better than equation 3.11, indicated by both percent difference and R^2. While the percent difference increases for most fits when compared to those of the 1.2" case, the average absolute difference does slightly decrease. The 0.4" case also offers improvement over the 1.2" case when a vortex center is located near a pressure sensor. As seen in Figure 3.10 and 3.11, there is a "jump" in the center locations when the vortex path crosses the sensors located at $y = 2.4$ that leads to more variability in the fits. This jump is mostly eliminated in Figure 3.15. The uncertainty and error in the 0.4" case could be further lowered by ignoring the last four or five columns of sensors. At these locations, the vortex moves off the array in some runs, where it cannot be located accurately.

Chapter 5

FUTURE WORK

5.1 Plasma Actuators

The plasma actuator model discussed above could be used to study the effects on a vortex by introducing a two-dimensional vortex to the initial conditions. But, in order to parametrically study these effects, the model will first need to either be improved or tuned to each case. If the model becomes a valid method to study plasma actuators, obtaining a high-voltage, high-frequency AC power supply would be required so that the experimental results match the model.

Further testing is required to examine effects of the location, properties, and orientation of the plasma actuator. The tests performed so far have been preliminary experiments to attempt to observe any change downstream of the actuator. Future tests should use with actuators with increased strength while varying the location and orientation to determine a configuration that produces a desired effect of stabilizing the vortex.

5.2 Vortex Detection

Future testing for vortex detection should focus on further decreasing the error in the measurements and on determining an optimum configuration. The pressure sensors used here were capable of measuring differential pressures in a much larger range than what was required. The maximum differential pressure measured in all runs was roughly 0.2 psid, whereas the sensors were capable of measuring a range of up to ± 5 psid. Sensors with a range closer to the 0.2 psid measured would decrease the error in the measurements. This would also open up the testing to a lower range of velocities, and therefore a more complete data set could be formed. The goal of this analysis should be to optimize the number and location of sensors to best locate a vortex. More tests should be run with a variety of spanwise sensor spacings to find a distance that is small enough to accurately resolve the

center, but large enough so that any unsteady effects of a flow will not move the vortex out of the measurement bounds. If only one spanwise set of sensors will be used, the distance they are located downstream of the vortex generator could also be optimized.

BIBLIOGRAPHY

[1] Shahab Shahinfar, Sohrab S. Sattarzadeh, Jens H. M. Fransson, and Alessandro Talamelli. Revival of classical vortex generators now for transition delay. *Physical Review Letters*, 2012.

[2] J. Reece Roth. Aerodynamic flow acceleration using paraelectric and peristaltic electrohydrodynamic effects of a one atmosphere uniform glow discharge plasma. *Physics of Plasmas*, 2003.

[3] Aline J. Cotel. *Entrainment and Detrainment of a Jet Impinging on a Stratified Interface*. PhD thesis, University of Washington, 1995.

[4] A. J. Cotel, J. A. Gjestvang, N. N. Ramkhelawan, and R. E. Breidenthal. Laboratory experiments of a jet impinging on a stratified interface. *Experiments in Fluids*, 1997.

[5] Gregory J Balle and Robert E Breidenthal. Stationary vortices and persistent turbulence in karman grooves. *Journal of Turbulence*, 2002.

[6] P. Ranjan and R. E. Breidenthal. Characteristics of an airfoil with stationary vortices. *International Journal of Emerging Multidisciplinary Fluid Sciences*, 2013.

[7] OR Dawson, M Bauer, GJ Balle, and RE Breidenthal. Relaminarization using stationary vortices.

[8] Matthias Bauer. Boundary layer turbulence measurements near a persistent streamwise vortex. Technical report, University of Washington.

[9] Eric Moreau. Airflow control by non-thermal plasma actuators. *Journal of Physics D: Applied Physics*, 2007.

[10] C. L. Enloe, Thomas E. McLaughlin, Robert D. VanDyken, K. D. Kachner, Eric J. Jumper, Thomas C. Corke, M. Post, and O. Haddad. Mechanisms and responses of a single dielectric barrier plasma actuator: Geometric effects. *AIAA Journal*, 2004.

[11] Dmitriy M. Orlov, Thomas C. Corke, and Mehul P. Patel. Electric circuit model for aerodynamic plasma actuator. In *AIAA Aerospace Sciences Meeting*, 2006.

[12] Thomas C. Corke, C. Lon Enloe, and Stephen P. Wilkinson. Dielectric barrier discharge plasma actuators for flow control. *Annual Review of Fluid Mechanics*, 2010.

[13] Dmitriy M. Orlov. *Modelling and Simulation of Single Dielectric Barrier Discharge Plasma Actuators*. PhD thesis, University of Notre Dame, 2006.

[14] G. Tathiri, E. Esmaeilzadeh, S. M. Mirsajedi, and H. Mahdavi Moghaddam. Experimental investigation of "why an ac dielectric barrier discharge plasma actuator is preferred to dc corona wind actuator in boundary layer flow control?". *Journal of Applied Fluid Mechanics*, 2014.

[15] M. Forte, J. Jolibois, J. Pons, E. Moreau, G. Touchard, and M. Cazalens. Optimization of a dielectric barrier discharge actuator by stationary and non-stationary measurements of the induced flow velocity: application to airflow control. *Experiments in Fluids*, 2007.

[16] Jérôme Pons, Eric Moreau, and Gérard Touchard. Asymmetric surface dielectric barrier discharge in air at atmospheric pressure: electrical properties and induced airflow characteristics. *Journal of Physics D: Applied Physics*, 2005.

[17] G. Correale, T. Michelis, D. Ragni, M. Kotsonis, and F. Scarano. Nanosecond-pulsed plasma actuation in quiescent air and laminar boundary layer. *Journal of Physics D: Applied Physics*, 2014.

[18] D. V. Roupassov, A. A. Nikipelov, M. M. Nudnova, and A. Y. Starikovskii. Flow separation control by plasma actuator with nanosecond pulsed-periodic discharge. *AIAA Journal*, 2009.

[19] Y. B. Suzen, P. G. Huang, J. D. Jacob, and D. E. Ashpis. Numerical simulations of plasma based flow control applications. In *AIAA Fluid Dynamics Conference and Exhibit*, 2005.

[20] A. Bouchmal. Modeling of dielectric-barrier discharge actuator. Master's thesis, Delft University of Technology, 2011.

Appendix A

MATLAB CODE FOR FINDING VORTEX CENTER

The following Matlab code uses seven methods to find the center of a vortex and plots those centers so they could be compared.

```
RUN = 2; %Choose run number
qNUM = 7; %Choose dynamic pressure (1=10Q, 2=20Q, etc...)

spacing = 0.4; %Set to equal sensor spacing [in]

for m=1:16

    %Cp_temp == differential Cp across spanwise row of sensors
    Cp_temp = Cp2(:,m,qNUM,RUN) - Cp2(:,m,qNUM,1) ;

    %Find peak point and two adjacent points
    [maxvalue,maxindex] = min(Cp_temp);
    if maxindex == 1
        maxindex = 2;
        maxvalue = Cp_temp(2);
    end
    if maxindex == 8
        maxindex = 7;
        maxvalue = Cp_temp(7);
    end
    points(1) = Cp_temp(maxindex-1);
    points(2) = Cp_temp(maxindex);
    points(3) = Cp_temp(maxindex+1);
    loc(1) = y2(maxindex-1);
    loc(2) = y2(maxindex);
    loc(3) = y2(maxindex+1);

```

```
28  %Set freestream velocity
29  U = v_6(qNUM-1)*12; %[in/s]
30
31  %Set fit limits for vortex height
32  h_min = 0.5; %[in]
33  h_max = 5.0;
34  h_set = 0.8;
35
36  %Create fit for Cp
37  Cp_fittype = fittype('-(Gamma*h/(pi*(h^2+(z-offset)^2)*U))^2',...
38      'independent','z','problem','U',...
39      'coefficients',{'Gamma','offset','h'});
40  %Create fit for Cp + y-offset, h variable
41  Cp_fittype_y = fittype(...
42      '-(Gamma*h/(pi*(h^2+(z-offset)^2)*U))^2 + yoffset',...
43      'independent','z','problem','U','coefficients',...
44      {'Gamma','offset','h', 'yoffset'});
45  %Create fit for Cp + y-offset, h set
46  Cp_fittype_y2 = fittype(...
47      '-(Gamma*h/(pi*(h^2+(z-offset)^2)*U))^2 + yoffset',...
48      'independent','z','problem',{'U','h'},'coefficients',...
49      {'Gamma','offset','yoffset'});
50
51  %%% Fit over entire row -- h=set %%%
52  fitobj1 = fit(y2(:),Cp_temp(:),Cp_fittype,'problem',U,'Lower',...
53      [0 0 h_set],'Upper',[5000 3.5 h_set],'StartPoint',...
54      [3000 y2(maxindex) h_set]);
55  %%% Fit over entire row -- h=variable %%%
56  fitobj2 = fit(y2(:),Cp_temp(:),Cp_fittype,'problem',U,'Lower',...
57      [0 0 h_min],'Upper',[5000 3.5 h_max],'StartPoint',...
58      [3000 y2(maxindex) h_min]);
59  %%% Fit over entire row + y-offset -- h=set %%%
60  fitobj3 = fit(y2(:),Cp_temp(:),Cp_fittype_y,'problem',U,'Lower',...
61      [0 0 h_set -1],'Upper',[5000 3.5 h_set 1],'StartPoint',...
62      [3000 y2(maxindex) h_set 0]);
63  %%% Fit over entire row + y-offset -- h=variable %%%
```

```
64      fitobj4 = fit(y2(:),Cp_temp(:),Cp_fittype_y,'problem',U,'Lower',...
65          [0 0 h_min -1],'Upper',[5000 3.5 h_max 1],'StartPoint',...
66          [3000 y2(maxindex) h_min 0]);
67      %%% Fit over 3 highest -- h=variable %%%
68      fitobj5 =fit(loc(:),points(:),Cp_fittype,'problem',U,'Lower',...
69          [0 0 h_min],'Upper',[5000 3 h_max],'StartPoint',...
70          [3000 y2(maxindex) 1]);
71      %%% Fit over 3 highest + y-offset -- h=set %%%
72      fitobj6 = fit(loc(:),points(:),Cp_fittype_y2,'problem',{U,h_set},...
73          'Lower',[0 0 -1],'Upper',[5000 3 1],'StartPoint',...
74          [3000 y2(maxindex) 0]);
75
76      %Extract center from each fit equation
77      center(m,1) = fitobj1.offset; %[in]
78      center(m,2) = fitobj2.offset;
79      center(m,3) = fitobj3.offset;
80      center(m,4) = fitobj4.offset;
81      center(m,5) = fitobj5.offset;
82      center(m,6) = fitobj6.offset;
83
84      %Extract height from each fit equation
85      h(m,1) = fitobj1.h; %[in]
86      h(m,2) = fitobj2.h;
87      h(m,3) = fitobj3.h;
88      h(m,4) = fitobj4.h;
89      h(m,5) = fitobj5.h;
90      h(m,6) = fitobj6.h;
91
92      %Extract circulation from each fit equation
93      Gamma(m,1) = fitobj1.Gamma; %[in^2/s]
94      Gamma(m,2) = fitobj2.Gamma;
95      Gamma(m,3) = fitobj3.Gamma;
96      Gamma(m,4) = fitobj4.Gamma;
97      Gamma(m,5) = fitobj5.Gamma;
98      Gamma(m,6) = fitobj6.Gamma;
99
```

```
100         %Ratio equation
101         ratio = (points(2) − min(points(1),points(3))) / ...
102             (points(2) − max(points(1),points(3)));
103         center(m,7) = loc(2) + 0.2∗(1−ratioˆ2) ∗ ((points(1)−points(3))/...
104             (abs(points(1)−points(3))));
105
106         %Determine mean center location from 7 methods
107         centeravg(m) = mean(center(m,:));
108
109         %Calculate percent difference normalized by spacing
110         for n = 1:7
111             diff(m,n) = abs(center(m,n) − centeravg(m))/spacing;
112         end
113     end
114
115     %Calculate average percent difference for each fit
116     for n = 1:7
117         diff_avg(n) = mean(diff(:,n));
118     end
119
120     %% Plotting
121
122     %Figure 1 − Plot center locations on spatial domain
123     figure
124     hold on, axis equal
125     marker = ['x' '∗' 'o' '+' 'd' 's' 'p'];
126     for n = 1:7
127         %Plot center locations on 2D spatial domain
128         plotnum1(n) = plot(x2,−center(:,n), marker(n));
129         plotnum1(n).MarkerEdgeColor = 'k';
130
131         %Plot lsline for each fit
132         linearfit = lsline;
133
134         %Calculate Rˆ2 correlation coeff for each fit
135         R2(n) = power(corr2(x2',center(:,n)),2);
```

```
136 end
137 for n=1:7
138     set(linearfit(n),'color','k')
139 end
140
141 %Plot sensor locations as .
142 plot(X2,-Y2,'.k')
143 ylim([-2.8 0])
144 xlim([0.5 15.5])
145 xlabel('x'), ylabel('y')
146
147 legend([plotnum1(1) plotnum1(2) plotnum1(3) plotnum1(4) plotnum1(5)...
148     plotnum1(6) plotnum1(7)],'Full Fit -- h=0.8',...
149     'Full Fit -- h=variable', 'Full Fit + y-offset -- h=0.8',...
150     'Full Fit + y-offset -- h=variable', '3 Sensor Fit -- h=variable',...
151     '3 Sensor Fit + y-offset -- h=0.8', 'Equation 3.11','Location',...
152     'NorthOutside');
153
154 %Figure 2 - Plot percent differences
155 figure
156 hold on
157 for n = 1:7
158     plotnum2(n) = plot(x2,diff(:,n).*100,marker(n));
159     plotnum2(n).MarkerEdgeColor = 'k';
160 end
161 xlim([0.5 15.5])
162 xlabel('x'), ylabel('% Difference')
```

Appendix B

C UDF CODE

The following C code was input into ANSYS Fluent as a user-defined function to implement the plasma actuator model.

```
1  #include "udf.h"
2  #include "math.h"
3  #include "sg_udms.h"
4  #define debye 0.001
5  #define rhomax 0.0008
6  #define phimax 5000
7  #define sigma 0.003
8  #define rholoc 0.0
9  enum {
10 phi,
11 rho
12 };
13 enum {
14 Ex,
15 Ey,
16 Fx,
17 Fy,
18 Fm };
19
20
21
22
23 DEFINE_ADJUST(udf_adjust, domain)
24 {
25 Thread *t;
26 cell_t c;
27 thread_loop_c(t,domain)
```

```
{
begin_c_loop(c,t)
{
 C_UDMI(c,t,Ex)=−C_UDSI_G(c,t,phi)[0];
 C_UDMI(c,t,Ey)=−C_UDSI_G(c,t,phi)[1];
}
end_c_loop(c,t)
}
}



DEFINE_SOURCE(rho_source, c, t, dS, eqn)
{
real source;
source=−pow(debye,−2)∗C_UDSI(c,t,rho);
dS[eqn]=−pow(debye,−2);
return source;
}



DEFINE_SOURCE(X_Source, c, t, dS, eqn)
{
real Sourcex;
 Sourcex=−rhomax∗phimax∗C_UDSI(c,t,rho)∗C_UDSI_G(c,t,phi)[0];
 dS[eqn]=−rhomax∗phimax;
 C_UDMI(c,t,Fx)=Sourcex;
 return Sourcex;
}



```

```
64  DEFINE_SOURCE(Y_Source, c, t, dS, eqn)
65  {
66  real Sourcey;
67   Sourcey=−rhomax∗phimax∗C_UDSI(c,t,rho)∗C_UDSI_G(c,t,phi)[1];
68   dS[eqn]=−rhomax∗phimax;
69   C_UDMI(c,t,Fy)=Sourcey;
70   C_UDMI(c,t,Fm)=sqrt(C_UDMI(c,t,Fx)∗C_UDMI(c,t,Fx)+C_UDMI(c,t,Fy)∗C_UDMI(c,t,Fy));
71   return Sourcey;
72  }
73
74
75
76
77  DEFINE_PROFILE(rho_profile,thread,i)
78  {
79  float r[3];
80  float x;
81  real xloc;
82  face_t f;
83  begin_f_loop(f,thread)
84  {
85  F_CENTROID(r,f,thread);
86  xloc = r[0];
87  F_PROFILE(f,thread,i)=exp(−pow((xloc−rholoc),2)/(2∗pow(sigma,2)));
88  }
89  end_f_loop(f,thread)
90  }
```